

When the Shadow Meets Its Measure: Assessing the Feasibility of Submillimeter Black Hole Shadow Imaging in Megamaser Disk AGN

ROMAN N. BURRIDGE¹ AND GEOFFREY C. BOWER^{2, 3, 1}

¹Department of Physics and Astronomy, University of Hawai'i at Mānoa, 2505 Correa Road, Honolulu, HI 96822, USA

²East Asian Observatory, 660 N. A'ohoku Place, Hilo, HI 96720, USA

³Institute of Astronomy and Astrophysics, Academia Sinica, 645 N. A'ohoku Place, Hilo, HI 96720, USA

ABSTRACT

Active galactic nuclei (AGN) hosting water megamaser disks enable exceptionally precise geometric determinations of black hole mass, distance, inclination, and dynamical center. In anticipation of upcoming space-based very long baseline interferometry missions, megamaser disk AGN offer a uniquely valuable probe of strong-gravity regimes through black hole shadow (BHS) imaging beyond Sgr A* and M87*. In this work, we (1) map the predicted BHS diameters of twenty-one of the most precisely characterized megamaser disk AGN to submillimeter-millimeter (submm-mm) interferometric baseline requirements, (2) estimate their respective AGN-core flux densities at submm-mm wavelengths, accounting for thermal-dust contamination, extended-jet emission, and intrinsic variability, and (3) determine the astrometric precision required to detect spin-dependent positional offsets between the BHS and the megamaser disk dynamical center. NGC 4258 stands out as the only megamaser disk AGN detectable on Earth-L2 baselines in the submm-mm regime, while other megamaser disk AGN in the sample would require baselines approaching Earth-L4/L5 distances; moreover, only a handful exhibit flux densities above ~ 10 mJy. Our results further indicate a submillimeter excess in NGC 4258, suggesting that the accretion disk remains thin down to a transitional radius of $\lesssim 100$ Schwarzschild radii, within which the flow becomes advection dominated. For a maximally spinning supermassive black hole in NGC 4258, we show that the astrometric precision of the BHS centroid necessary to detect the BHS-dynamical center offset could, in principle, be achieved with Earth-Moon baselines; however, it would also demand astrometric precision of the water maser dynamical center roughly fifty times better than what is currently attainable.

Keywords: Megamasers ; Water masers ; Active galactic nuclei ; Black hole physics ; VLBI ; Astrometry ; Millimeter astronomy ; Submillimeter astronomy

1. INTRODUCTION

Measuring black hole (BH) masses is fundamental both to astrophysics and to tests of general relativity. Mass determines the gravitational radius that defines the event horizon, and recent horizon-scale imaging has resolved the black hole shadow (BHS)¹ in M87* and Sagittarius A*, in agreement with the predictions of gen-

eral relativity (Event Horizon Telescope Collaboration et al. 2019f, 2022d,e,f). Mass also anchors the scaling relations that link supermassive black holes (SMBH) to the growth of their host galaxies, and sets the Eddington limit that regulates accretion and feedback (Kormendy & Ho 2013; Fabian 2012; Heckman & Best 2014). Traditional dynamical methods, including stellar and gas kinematics, reverberation mapping, single-epoch virial methods, and even water megamaser disk systems, probe the motions of tracers in the gravitational potential to infer a BH mass estimate. By contrast, very long baseline interferometry (VLBI) achieves horizon-scale resolution and delivers a geometric probe of space-time itself.

rburr@hawaii.edu

¹ We use ‘BHS’ to refer to the region on the observer’s screen corresponding to photons that are captured by the BH, leaving a dark area against the surrounding emission. It is circular in the Schwarzschild case, and displaced or distorted by spin and inclination in the Kerr case.

Direct imaging of a BHS using VLBI at submillimeter-millimeter (submm-mm) wavelengths requires that the emission of the AGN-core surrounding the SMBH be (1) large enough in angular size to be resolved by the interferometric baseline, (2) sufficiently bright, and (3) optically thin at the observing frequency. In this work, we evaluate AGN hosting water megamaser disks in terms of their predicted angular BHS sizes and the flux densities of their AGN-cores in the submm-mm regime, two fundamental parameters governing the feasibility of BHS-scale VLBI imaging.

We define our sample as the twenty-one megamaser disk AGN with the most precise and complete measurements of SMBH mass, distance, and inclination derived from VLBI disk modeling (Greene et al. 2016) (Table 2). Their well-constrained masses and distances enable the direct calculation of the expected BHS angular size (Pesce et al. 2021):

$$\theta_{\text{BHS}} = \sqrt{27} \frac{R_S}{D_{\text{SMBH}}}, \quad R_S = \frac{2GM}{c^2} \quad (1)$$

where M is the BH mass, D_{SMBH} is its distance from Earth, R_S is the Schwarzschild radius, and the prefactor $\sqrt{27}$ corresponds to a Schwarzschild BH (Bardeen 1973). The resulting angular BHS size, θ_{BHS} , is exceedingly small – the largest source, NGC 4258 (0.62 μas), would require a baseline roughly 30 times the diameter of the Earth, implying that space-based VLBI (SVLBI) is necessary. Values of θ_{BHS} for the water maser sample are listed in Table 2. This outcome is consistent with previous analyses across the entire AGN population: beyond M87* and Sgr A*, resolving the BHS of the next largest source (megamaser disk AGN or not) will require baselines approximately twice Earth’s diameter in the submm-mm regime (Zhang et al. 2025).

To assess the VLBI baselines required to resolve the BHS of our set of megamaser disk AGN, we estimate the angular resolution of several earth to space baselines using the diffraction limit:

$$\theta_{\text{VLBI}} = \frac{\lambda}{D_{\text{BL}}} \quad (2)$$

where θ_{VLBI} is the interferometric fringe spacing, λ is the observing wavelength, and D_{BL} is the interferometric baseline length. We adopt 230 GHz as the reference frequency when calculating the baseline resolving power. In addition to the Earth-diameter baseline achieved by the EHT, we consider prospective submm-mm interferometric configurations that have been proposed to launch within the next decade: *BHEX*, *Millimetron*, and *Origins*; as well as the already launched cm interferometric mission *LOVEX* (Johnson et al. 2024; Andrianov

et al. 2020; Syachina et al. 2024; Pesce et al. 2019; Hong et al. 2025). The *BHEX* baseline is less than 10 times the Earth-Moon distance and only marginally achieves $\theta_{\text{BHS}} \lesssim \theta_{\text{VLBI}}$ for even the largest BHS beyond M87* and Sgr A* (Issaoun et al. 2024; Akiyama et al. 2024). *LOVEX* is located at the Earth-Moon baseline. *Millimetron* and *Origins* are proposed to operate with baselines extending from Earth to L2 (Andrianov et al. 2020; Pesce et al. 2019). For completeness, the Earth-L4/L5 baseline serves as a fiducial long-baseline geometry capable of resolving all BHS in our megamaser disk AGN sample.

This yields approximate angular resolutions of (1) 21.1 μas for an Earth-diameter baseline (12,756 km), (2) 10.1 μas for *BHEX* (20,200 km), (3) 0.69 μas for the Earth-Moon distance (382,500 km), (4) 0.18 μas for the Earth-L2 distance (1.5 million km), and (5) 0.0018 μas for the Earth-L4/L5 distance (150 million km).

Missions such as *Millimetron* or *Origins* would be able to resolve only the BHS of NGC 4258 from the megamaser disk AGN sample. The next largest BHS, NGC 1194 and NGC 1068, would require an increase in baseline distance to ~ 1.5 times the distance from Earth to L2. The BHS of the entire water maser-AGN sample would be resolved with a baseline extending from Earth to L4/L5 – a fiducial yet optimistically achievable configuration for humanity. In addition to these megamaser disk AGN, we also evaluate NGC 3079, NGC 4945, and Circinus, which stand out as the brightest of the water maser sample.

Having considered the baseline and flux requirements for resolvability, it is also essential to consider how inclination influences the appearance of the BHS. Inclination couples with spin and optical depth to determine the degree of asymmetry in the observed image, introducing a fundamental degeneracy among these three parameters² (Takahashi 2004). In the fully optically thick regime, the BHS is completely obscured and cannot be recovered. In the moderately optically thin regime, photon rings³ remain inaccessible, but the BHS becomes marginally resolvable as synchrotron photons from the hot, magnetized flow begin to escape (Inoue & Doi 2014). At shorter wavelengths, as the emission becomes increasingly optically thin, the photon ring can be resolved

² In a moderately optically thick regime, a non-spinning SMBH viewed edge-on appears semicircular, whereas in the optically thin regime, the BHS remains circular regardless of inclination. In both cases, spin introduces asymmetries and a centroid displacement.

³ Photon rings are photons that orbit near the critical curve before escaping, forming thin rings that converge exponentially onto the BHS’s edge.

(Bronzwaer et al. 2020; Salehi et al. 2024). Each successive subring is progressively demagnified, rotated, and time-delayed relative to the last, and recovering the corresponding observables – the Lyapunov exponent, time delay, and azimuthal shift – requires a reliable determination of inclination. Sub-parsec inclination and polarization measurements of water megamasers additionally constrain the magnetic field structure in AGN (Gallimore et al. 2024). Furthermore, comparing the maser-disk inclination to orientations measured on 10-100 pc scales can reveal whether the inner disk aligns with circumnuclear gas or with the BH spin axis, thereby helping to distinguish whether the system resides in a standard and normal evolution (SANE) or magnetically arrested disk (MAD) magnetic flow state (Ressler et al. 2023).

Inclination is difficult to extract from VLBI images of Sgr A* because of degeneracies with accretion and outflow properties. For M87*, it must be inferred from the jet axis rather than from the BHS itself (Event Horizon Telescope Collaboration et al. 2021b, 2022f). Estimates from other tracers span widely different spatial scales – stellar disks on kiloparsec scales, molecular gas on hundreds of parsecs, and infrared or X-ray obscurers on parsec scales – and carry large uncertainties (Efstathiou et al. 2021; Murphy et al. 2011; Brightman & Nandra 2011). By contrast, water maser disks provide sub-parsec geometric measurements of inclination with < 1% precision (Humphreys et al. 2008; Gallimore et al. 2024).

Stellar and gas dynamical models can, in principle, also constrain the mass, inclination, and position of the dynamical center; however, they are limited by degeneracies such as orbital anisotropy and can be biased by turbulence, inflows, or outflows that depart from pure rotation. Reverberation mapping and single-epoch virial methods depend on average assumptions about broad-line geometry, kinematics, and orientation, which may not hold for individual objects. By contrast, 22 GHz water maser disks follow a straightforward geometric model, directly tracing Keplerian rotation in molecular disks on sub-parsec scales through a collisionally pumped population inversion that amplifies the background AGN signal. This requires a warm (~ 300 - 1000 K), dense ($n_{\text{H}_2} \sim 10^7$ - 10^{11} cm $^{-3}$) medium with a sufficiently large H₂O column density and velocity coherence along the line of sight (Lo 2005).

Mass uncertainties for key megamaser disk AGN include: NGC 4258 (7%), NGC 3079 (10%), Circinus (23%), NGC 1068 (<1%), NGC 1194 (10%), and NGC 4945 (40%) (Greene et al. 2016; Zhang et al. 2024). These uncertainties are comparable to those reported by

the Event Horizon Telescope Collaboration (EHTC) for M87* and Sagittarius A* and are also consistent with mass estimates from gas and stellar dynamical modeling in M87*, which range from roughly \sim 6-20% (Walsh et al. 2013; Liepold et al. 2023; Simon et al. 2024; Gebhardt et al. 2011), although they remain less precise than estimates from stellar orbital constraints for Sgr A* – 0.28% (GRAVITY Collaboration et al. 2022) and 1.8% (Do et al. 2019). The value of water maser targets also lies in their ability to enable direct comparisons between water maser-based masses and stellar or gas dynamical estimates, as in the rare cross-checking studies of Thater et al. (2021), which help to quantify systematic uncertainties. This advantage extends to all our key sources, for which X-ray spectra provide a complementary means of refining the BH mass and inclination using priors derived from water maser geometry. In this way, X-ray spectral modeling can cross-check both parameters and evaluate the consistency between dynamical and radiative methods, as demonstrated for NGC 4258 (Gliozzi et al. 2021; Trześniewski et al. 2011; Yang et al. 2007).

This paper is organized as follows. Section 2 describes the archival compilation of SMBH mass, distance, and inclination; newly conducted SMA observations; ALMA and VLA archival compilation; and CASA fitting for continuum extraction. Section 3 presents the primary candidates of megamaser disk AGN for BHS imaging using SVLBI; the required astrometric precision in the BHS image and in megamaser disk measurements of the dynamical center that is necessary to detect spin-dependent offsets between the BHS and the dynamical center; and the flux densities of the sample at submm-mm wavelengths, accounting for thermal-dust contamination, extended-jet emission, and intrinsic variability. Section 4 provides source-by-source discussions of NGC 4258, NGC 1194, NGC 3079, NGC 4945, Circinus, and NGC 1068. Section 6 summarizes our conclusions.

2. DATA COLLECTION

This section outlines the data used in the analysis. Section 2.1 compiles SMBH masses and distances that are used to compute the BHS sizes; Section 2.2 presents the new SMA observations; Section 2.3 describes the archival ALMA and VLA compilation and how we select, for each source, the reference frequency ν_0 in the submm-mm regime; and Section 2.4 describes the gaussian fitting procedure used to ensure uniform continuum extraction.

2.1. Mass Distance, and Inclination

We define our sample as the twenty-one megamaser disk AGN with the most precise and complete measurements of SMBH mass, distance, and inclination derived

from VLBI disk modeling (Greene et al. 2016). The angular size of a BHS depends on the mass of the SMBH and its distance from Earth, as listed in Table 2. These parameters, compiled from the literature, are used to calculate the BHS diameters shown along the horizontal axis of Figure 1, following Equation 1. Mass measurements are primarily taken from Greene et al. (2016). Distances are obtained from the NASA/IPAC Extragalactic Database (NED); for sources with $z < 0.0015$, redshift-independent distances are used, while for higher redshifts, distances are derived from redshift, assuming a Hubble constant of $H_0 = 73.9 \pm 3.0 \text{ km s}^{-1} \text{ Mpc}^{-1}$ (Pesce et al. 2020b). When available, water maser-based distances are preferred (Pesce et al. 2018); otherwise, the estimate with the smallest reported uncertainty is adopted. Water maser determined inclination angles are also reported. Following the convention of (Zhang et al. 2024), some inclinations in Table 2 do not have associated uncertainties, as they were fixed during the kinematic modeling; If a maser paper does not state an inclination, we assume that the inclination is fixed at 90 °. For NGC 1320 and NGC 4388, the absence of systematic water maser components limits the reliability of these orientation estimates (Kuo et al. 2010; Gao et al. 2016b).

2.2. SMA Observation and Calibration

We conducted submm-mm continuum observations using the Submillimeter Array (SMA) on Maunakea in the subcompact configuration on 2023 March 16 under good weather conditions, with precipitable water vapor (PWV) below 4 mm, under program 2022B-H002. Out of 8 antennas, antenna2 and antenna7 were unavailable. The lower sideband ranges from 209.4-221.7 GHz, and the upper sideband at 229.4-241.7 GHz; corresponding to a 24.6 GHz of continuous bandwidth. Each side band consists of 6 – 2.3 GHz bandwidth – spectral windows. Of the 21 sources in our sample, 15 were observed. J0437+2456, IC 2560, NGC 3393, and CGCG 074-064 were not included in this run, and Circinus and NGC 4945 were outside the observable range. The synthesized beam-size was approximately 5-6 arcseconds full width half maximum (FWHM). Calibration began with 3C84 (bandpass) and Uranus (flux) and concluded with 3C279 (bandpass) and Ceres (flux). Phase calibrators were selected based on flux density ($\geq 0.5 \text{ Jy}$) and angular separation ($\leq 15^\circ$) from each science target.

Additionally, we conducted an additional submm-mm observation for NGC 4258 using the SMA on 2022 Jan 31 under satisfactory weather conditions, with PWV $\leq 4 \text{ mm}$, under program 2021B-H004. Out of 8 antennas; antenna3 and the lower sideband for antenna2

were unavailable. The lower sideband ranges from 219.4-231.7 GHz, and the upper sideband at 239.4-251.7 GHz. The synthesized beam-size was approximately 3 arcseconds. The flux calibrator chosen for this observation was MWC 349a, and the bandpass calibrator was 3C 279.

We calibrated and imaged the raw visibility data in CASA⁴. In addition to flagging edge channels, we flag the common extragalactic molecular line regions that are brighter than 1 Jy from (Martín et al. 2021). We account for redshift distances as listed in Table 2. These include C¹⁸O at 226.66, ¹³CO at 226.874, CN at 226.875, CO at 230.538, and CS at 244.936. To account for line broadening, all channels within $\pm 300 \text{ km s}^{-1}$ of each transition in the rest frame – corresponding to a frequency width of approximately 0.9-2.2 GHz in the observed frame – are excluded from the fit (Martín et al. 2021). This corresponds to flagging 4-9% of the 24.6 GHz continuous bandwidth.

The reference antenna was set to antenna8, which established a zero point for the phase. To correct for short-term variations, we set the "short" solution interval to one solution per integration time, and to correct for long-term variations, we set the "long" solution interval to the length of an entire scan. For a given frequency channel and antenna, we required the calibration tables to retain only solutions for which at least three baselines successfully produced solutions. We also required a minimum signal-to-noise-ratio (SNR) of 2 for phase calibration and 3 for amplitude calibration.

First, the bandpass calibration table, 3C 279, was generated from the bandpass calibrator while self-calibrating for short-term phase variations. Long- and short-term phase calibration tables were then generated for the phase, flux, and bandpass calibrators while applying the bandpass table. In order to maximize the SNR of the continuum image, spectral windows were combined in the upper and lower sidebands. To obtain separate images for the upper and lower sidebands for spectral-index extraction, the spectral windows were grouped into symmetric sub-sidebands. Then, long-term amplitude calibration tables are generated for the phase, flux, and bandpass calibrators while applying the short-term phase and bandpass correction tables. Then, the flux calibrator was fixed at its known brightness to establish an absolute flux scale across the bandwidth, and flux calibration tables were generated for the phase and bandpass calibrators. The flux calibrator for 2022B-H002 was Uranus and was modeled using the Butler-

⁴ SMA reduction is outlined in https://lweb.cfa.harvard.edu/rtdc/SMAdata/process/tutorials/sma_in_casa_tutorial.html

JPL-Horizons 2012 flux standard. The flux calibrator for 2021B-H004 was MWC 349a was assigned a manual flux density of 1.98 Jy based on its value in the SMA Calibrator Catalog.

Bandpass, phase, and flux tables were then applied to all fields. Science fields use long-phase calibration corrections, while the calibrator fields use short-phase calibration corrections. The data were then deconvolved to form a continuum image, with no CLEAN iterations applied to the calibrators, while the science targets were deconvolved with 10 iterations. The brightness of the calibrators was then checked against known values to ensure that a proper flux scale had been established.

2.3. Archival Collection for Continuum Flux Measurements

To supplement our SMA observations, we retrieved archival continuum images from the Atacama Large Millimeter/submillimeter Array (ALMA) and Karl G. Jansky Very Large Array (VLA) data archives. For each observation, we obtain the synthesized beam size—defined as the geometric mean of the FWHM semi-major and semi-minor axes of the synthesized beam – and frequency from the CASA task imhead. We assume that these parameters correspond correctly to their respective observations; otherwise, issues would arise in the analysis presented in Sec 3. For example, if the upper sideband had been flagged prior to data reduction without updating the final header published in the respective archive, the frequency used in Tables 3,4 would need to be updated.

For NGC 4258, additional flux density measurements were taken from Nobeyama Millimeter Array (NMA) observations at 96 and 347 GHz, as well as from SCUBA on the James Clerk Maxwell Telescope (JCMT) (Doi et al. 2005). We also included archival VLA observations at 33 GHz from (Kamali, F. et al. 2017).

2.4. CASA Fitting and Graph Production

We fit two-dimensional Gaussians to all images in CASA, fixing the Gaussian size and position angle to those of the synthesized beam. The Gaussian centroid is initially allowed to vary within a $10''$ box centered on the J2000 NED coordinates obtained using the astroquery.ipac.ned.Ned function. The J2000 and ICRS coordinate systems can differ by as much as $0.02''$. Because ALMA uses the ICRS frame and the beam size in our data set is as small as $0.014''$ (for the ν_0 image of NGC 1068 listed in Table 10), the J2000 coordinates were converted to the ICRS frame using CASA’s analysisUtils.au.J2000ToICRS function when performing ALMA fits.

Given the non-uniform frequency coverage and beam-sizes in our dataset, we identify, for each source, the detection with the smallest beam within the 200-400 GHz range as the reference frequency, ν_0 , interpreting it as the best probe of the AGN-core in the submm-mm VLBI regime. The corresponding values are plotted on the vertical axis of Figure 1. Note that ν_0 could not be found for CGCG 074-064 or J0437+2456.

If ν_0 refers to an observation with a synthesized beam < 1 , then we re-analyze that dataset: the fitting region is a box aligned with and rotated to the 3σ beam-size (converting FWHM to 3σ using $\theta_{3\sigma} = 3\theta_{\text{FWHM}}/(2\sqrt{2 \ln 2})$, centered at the Gaussian centroid from the ν_0 image.

If ν_0 could not be found, or if it refers to a detection with a synthesized beam ≥ 1 , then the fitting region is centered at the location from NED and is twice the 3σ beam-size.

Within the fitting region, the centroid of the gaussian fit are allowed to vary while the size and rotation are fixed to that of the synthesized beam. In order to account for extended emission, a compactness analysis would need to be conducted; however, the sparse sampling of time and beam-size in our dataset introduces degeneracy between variability and compactness (See Section 5).

A source is considered detected if the fit converges and the SNR exceeds 3; otherwise, it is treated as a non-detection. For non-detections with $\nu_0 < 1$, an upper limit is assigned as three times the root mean square (RMS) noise measured within a region matching the beam-size at the source position. For non-detections with $\nu_0 > 1$ or without ν_0 , the upper limit is assigned as three times the RMS noise measured within the fitting region (twice the 3σ beam-size).

3. RESULTS AND ANALYSIS

This section assesses the feasibility of near-future SVLBI in resolving the water maser sample. Section 3.1 presents the new SMA results. Section 3.2 presents the primary candidates on the BHS-size-versus-flux plane (Figure 1) and discusses the ability to image the BHS of the primary candidates of proposed SVLBI mission concepts in terms of resolution and sensitivity. Section 3.3 quantifies the required astrometric precision in the BHS image and in megamaser disk measurements of the dynamical center that is necessary to detect spin-dependent offsets between the BHS and the dynamical center. Section 3.4 extrapolates upper limits for contamination in the submm-mm regime from low-frequency extended-jets and high-frequency thermal-dust, while Section 3.5 examines variability.

3.1. SMA results

SMA detections that correspond to ν_0 (Sec 2.3) include NGC 4258, NGC 2273, and NGC 3079. SMA detections that do not correspond to ν_0 include NGC 1068, and NGC 4388.

SMA non-detections that correspond to ν_0 include Mrk 1029, NGC 2960, NGC 6264, NGC 6323, UGC 3789 and UGC 6093. SMA non-detections that do not correspond to ν_0 include ESO 558-G009, NGC 1194, NGC 1320, and NGC 5765b. Specific values can be found in Table 3.

3.2. Primary Candidates for SMBH Imaging using VLBI

Having established the baseline resolution and sensitivity requirements, we now identify which megamaser disk AGN are most promising for direct BH shadow imaging. Our assessment of primary candidates evaluates resolvability by considering both the size and brightness of each source. We additionally place these results in the context of proposed and fiducial SVLBI mission concepts.

For evaluating the feasibility of SVLBI, 230 GHz is adopted as the reference frequency and serves as the benchmark frequency for calculating baseline resolving power using Equation 2. This yields approximate angular resolutions of: (1) 21.1 μ as for an Earth-diameter baseline, (2) 10.1 for BHEX, (3) 0.69 μ as for the Earth-Moon distance, (4) 0.18 μ as for the Earth-L2 distance, and (5) 0.0018 μ as for the Earth-L4/L5 distance.

VLBI sensitivity can be estimated using Equation 3, which defines the theoretical thermal noise, ΔS_{ij} , for a given baseline (Walker 1995):

$$\Delta S_{ij} = \frac{1}{n_s} \sqrt{\frac{SEFD_i SEFD_j}{2\Delta t \Delta \nu}} \quad \text{Jy} \quad (3)$$

where $SEFD_{i,j}$ are the system equivalent flux densities (Jy) of the two antennas forming the baseline; n_s is the system efficiency factor; Δt is the coherent integration time (s); and $\Delta \nu$ is the observing bandwidth (Hz).

The SEFD for *Millimetron* is estimated to be 4000 Jy, while that for the SMA phased with ALMA is 74 Jy (Likhachev et al. 2022; Event Horizon Telescope Collaboration et al. 2019b). *Millimetron* is expected to operate with a bandwidth of $\Delta \nu = 4$ GHz, and the integration time is limited by the coherence timescale of ground-based telescopes due to atmospheric fluctuations, estimated as $\Delta t = 10$ s (Syachina et al. 2024). Under these parameters, the thermal noise is $1.9/n_s$ mJy, where n_s is the system efficiency factor, typically dominated by quantization losses in VLBI. For 2-bit quantization ($n_s = 0.88$), this corresponds to an SNR of 4.6 for a 10 mJy source (Novikov et al. 2021). Using these representative parameters and the sensitivity relation given

by Equation 3, the adopted flux-density thresholds of 1, 10, and 100 mJy correspond, respectively, a fiducial sensitivity capable of resolving the majority of BHS in our sample, a sensitivity of robust detection (SNR $\tilde{4.6}$), and a regime that remains insufficient to detect any water maser sources without a spaceborne hydrogen maser but is fully capable of detecting Sgr A* and M87*.

The coherence limitations of ultra-stable quartz oscillator (USO) SVLBI clocks are comparable to those set by atmospheric stability on ground-based baselines. At 230 GHz, integration times of up to 10 s are theoretically achievable for SVLBI using USO clocks, avoiding the need for heavier and more costly maser clocks (Burt et al. 2025). Integration times of 7 s have already been demonstrated at this frequency, sufficient to ensure that the measurement is limited by the true signal.

The coherence time on a space-ground baseline is jointly constrained by the stability of the onboard clock at the space station and by atmospheric phase variations at the ground station. Recent proposals suggest that source-frequency phase referencing (SFPR) systems, employing simultaneous multi-frequency observations (e.g., 86/230/345 GHz), could mitigate atmospheric fluctuations on the ground, potentially extending coherence times from 10 s to nearly an hour and reducing the theoretical thermal noise to below 0.1 mJy (Jiang et al. 2022). If atmospheric coherence on the ground is improved through SFPR, the bottleneck then shifts to the onboard clock; in this regime, any further gains in coherence time would require a spaceborne hydrogen maser.

With the resolvability and sensitivity regimes established, Figure 1 illustrates the resulting observational constraints, presenting BHS size and flux density estimates for each source, with M87 and Sgr A* included for comparison. Angular BHS sizes are computed from the SMBH mass and distance values in Table 2, while flux densities are drawn from the reference frequency observation; for M87* and Sgr A*, fluxes are adopted from Chen et al. (2023) and Wielgus et al. (2022), respectively. Vertical lines mark the angular resolutions corresponding to Earth-diameter, Earth-Moon, Earth-L2, BHEX, and Earth-L4/L5 baselines. Sources to the right of a given line are resolvable with that baseline. Horizontal lines show nominal VLBI sensitivity thresholds of 1, 10, and 100 mJy, with sources above a given line exceeding that threshold.

NGC 4258 stands out with the largest angular BHS in the sky. At 230 GHz, an Earth-L2 baseline provides a fringe spacing of ~ 0.18 μ as, sufficient to resolve its predicted BHS diameter of 0.617 ± 0.049 μ as (Table 2). Even an Earth-Moon baseline approaches the

required resolution. NGC 4258 is therefore the only known megamaser disk AGN resolvable with Earth-L2 baselines, making it the most accessible candidate in the sample for space VLBI imaging. Its AGN-core brightness has been measured as ~ 7 mJy beam $^{-1}$ at 226 GHz with the SMA (Table 5).

All other megamaser disk AGN require baselines longer than Earth-L2, with Earth-L4/L5 separations serving as an illustrative upper bound sufficient to resolve the majority of their predicted BHS. Among these, NGC 1194 and NGC 1068 exhibit the largest predicted BHS. Although not among the largest, the brightest submm-mm sources additionally include NGC 3079, NGC 4945, and Circinus.

3.3. Constraining the SMBH Spin Parameter using SVLBI

Where dual-band receivers allow SFPR, a mm-submm image could be directly tied to the 22 GHz water masers, calibrating the BHS to the water maser-traced center of mass (COM) and enabling a spin constraint from their relative offset without (Takahashi 2004; Bronzwaer et al. 2020). If SFPR is not available, a similar result can be achieved by observing both bands simultaneously and referencing them to the same calibrators. These calibrators are defined by the International Celestial Reference Frame (ICRF), which provides the standard coordinate system for the sky.

In principle, this alignment would be far simpler if water maser emission were present at submm-mm frequencies near the continuum band, since submm water masers could be referenced directly to the submm-mm image without requiring cross-band calibration between 22 and 230 GHz. Such same-band detection would avoid the systematic errors introduced by cross-band calibration and would provide a more stable astrometric reference for measuring the BHS-water maser offset, thereby motivating searches for submm-mm water maser transitions. Although many maser transitions are often not bright enough to probe extragalactic AGN, in certain cases they have been observed with luminosities exceeding those of the 22 GHz transition (Gray et al. 2015). For instance, 658 GHz water masers have been both modeled and detected in several asymptotic giant branch (AGB) stars, as well as in VY CMA (Menten & Young 1995), where the luminosity of 658 GHz lines surpassed that of their 22 GHz counterparts (Nesterenok 2015). 183 GHz lines have been detected in NGC 1194, NGC 3079, NGC 4945, and Circinus, but not in NGC 1068 (Pesce et al. 2023; Humphreys et al. 2005; Humphreys et al. 2016). 321 GHz lines have been detected in NGC 4945 and Circinus, but not in

NGC 1068 (Hagiwara et al. 2021; Pesce et al. 2016). 439 GHz emission has been detected in NGC 3079 (Humphreys et al. 2005).

The maximal offset between the BHS and the water maser-dynamical center is $\simeq 0.725, R_S$ for an extreme Kerr BH viewed edge-on. Equivalently, this corresponds to ≈ 0.14 times the BHS diameter (Takahashi 2004; Bronzwaer et al. 2020). The size of the maximal BHS-megamaser disk dynamical-center offset can be predicted from the SMBH mass and the distance measured via water maser kinematics. Substituting the expression for R_S from Equation 1 and applying the small-angle approximation to express the angular shift on the plane of the sky yields $\theta_{\text{shift}} = 0.725\theta_{\text{BHS}}/\sqrt{27}$.

For the case of NGC 4258, the largest source in the sample, detecting the maximal BHS-megamaser disk dynamical-center offset of $\theta_{\text{shift}} \approx 0.09$ μas requires an astrometric precision of $\sigma_\theta \approx 0.086 \pm 0.007$ μas . The baseline, observing frequency, and SNR necessary to achieve this precision can be determined using the positional uncertainty relation given in Equation 1 of Reid et al. (1988):

$$\sigma_\theta = \left(\frac{4}{\pi}\right)^{1/4} \frac{\theta_{\text{VLBI}}}{\sqrt{8 \ln 2}} \frac{1}{\text{SNR}} \quad (4)$$

Here, θ is given in Equation 2. For an Earth-Moon configuration at 230 GHz – with $\theta_{\text{VLBI}} \approx 0.69$ μas – would require a SNR of 3.6 ± 0.3 . So we arrive at the interesting result that, even though the BHS for NGC 4258 is not resolvable at Earth-Moon baselines (See Figure 1), the centroid of the BHS may be precise enough to obtain the BHS-megamaser disk dynamical-center offset.

To detect such an offset, the water maser-traced dynamical center must also be determined with comparable astrometric precision, i.e., $\sigma_\theta \lesssim 0.09\mu\text{as}$. From 22 GHz water maser VLBI measurements, Reid et al. (2019) determined the dynamical center's x-position as -0.152 ± 0.003 mas and y-position as 0.556 ± 0.004 mas. The resulting radial offset from the coordinate origin is $\sqrt{x^2 + y^2} = 0.576 \pm 0.005$ mas, corresponding to an uncertainty of approximately 5 μas . Therefore, an improvement in precision by a factor of ~ 55 would be required to resolve the maximal BHS-megamaser disk dynamical-center offset.

The ~ 5 μas precision of the water maser-traced COM reported by Reid et al. (2019), achieved using ground-based 22 GHz VLBI, provides a benchmark for current astrometric capability. Since an Earth-L2 baseline is approximately 120 times longer than the Earth's diameter, it may be feasible to achieve positional accuracies on the order of ~ 0.09 μas for the dynamical center using SVLBI. While extending baselines to Earth-L2 geome-

tries reduces the synthesized beam-size to $\lesssim 0.2 \mu\text{as}$, systematic errors in the determination of the water maser dynamical center are unlikely to scale proportionally. Water maser spot variability, turbulence in the disk, and amplification geometry may bias the fitted COM at the $\sim 0.1 \mu\text{as}$ level, independent of interferometric resolution. Thus, while a formal accuracy of $\sim 0.1 \mu\text{as}$ may, in principle, be achievable with Earth-L2 space VLBI, the true limiting factor is likely to be systematic error in COM determination rather than thermal noise.

In conclusion, SMBH spin could, in principle, be measured from the BHS-megamaser disk dynamical-center offset; however, such measurements will require SVLBI. An Earth-Moon baseline at 230 GHz could, under ideal conditions, resolve the BHS centroid; however, constraining the dynamical center to sub- μas precision with water maser observations will likely be limited by dominant systematic errors.

3.4. Estimating contamination from thermal-dust and extended-jets

We estimate potential contamination at ν_0 by extrapolating the flux density using a spectral-index α defined by $S_\nu \propto \nu^\alpha$, where S_ν is the flux density at frequency ν . We only examine observations offset by $\gtrsim 10\%$ above and $\lesssim 10\%$ below ν_0 , since such offsets accentuate the spectral slope and enable a clearer separation between rising thermal-dust emission and falling extended-jet emission. Smaller frequency differences are reserved for variability analysis. In Section 4, we present the thermal-dust and extended-jet upper limits that bound contamination at ν_0 . We also discuss signatures of variability (Section 3.5) and incorporate the corresponding upper bounds as a systematic uncertainty in both the submm-mm flux and the extended-jet contamination estimates.

To estimate contamination from high-frequency thermal-dust, we model it as a modified black body, $S_\nu = A\nu^{\beta+3}/(e^{h\nu/(kT)} - 1)$ (Casey 2012). T is the dust temperature, β is the dust emissivity index, which is set to 1.5, and A is a normalization constant that absorbs all physical factors determining the absolute flux level. In the cold molecular region, galactic dust can reach temperatures as low as 20 K, whereas in the warm molecular region, dust temperatures can reach up to 2000 K (Bolatto et al. 2013; Riffel et al. 2013). From the $e^{h\nu/(kT)} - 1$ factor in S_ν , one can see that in the mm-submm regime, the dust emission from the warm molecular region is ~ 130 times brighter than that from the cold emitting region. Since cold molecular regions exist on the order of tens of thousands of parsecs, and warm molecular regions exist on the order of hundreds

of parsecs, both regions are resolved by the observations presented in this paper (See the SED plots in Section 4). Therefore, we model thermal-dust contamination from a warm molecular region, where the $e^{h\nu/(kT)}$ term is negligible at temperatures of 2000 K, so that we can simply model thermal-dust with a spectral-index of $\alpha = +4.5$ (Rybicki & Lightman 1979).

For thermal-dust extrapolations, we use only measurements at frequencies $\gtrsim 10\%$ above ν_0 . Each higher-frequency measurement is projected downwards to ν_0 . The emitting region of the warm molecular region is assumed to be resolved, so we additionally apply beam-size corrections. If only one thermal-dust-emission component were present, all projected values would coincide. With this interpretation, any mismatch indicates an excess of non-dust emissions. We therefore take the lowest extrapolation as the upper limit.

Complementary to the high-frequency thermal-dust estimate, we assess low-frequency extended-jet⁵. We use measurements at frequencies $\lesssim 10\%$ below ν_0 and project each upward to ν_0 , assuming a synchrotron power-law index $\alpha = -0.5$ (Rybicki & Lightman 1979; Blandford & Ostriker 1978). Treating the extended-jet as smaller than the smallest beam-size –consistent with VLBI studies of the water maser-AGN sample – we apply no beam-size correction. As above, we adopt the smallest projected flux density at ν_0 as a strict upper limit on the extended-jet contribution. Unlike thermal-dust, extended-jet emission is variable, and we account for this by incorporating variability upper bounds as systematic uncertainties in the extended-jet extrapolations when possible (Section 3.5).

Where low-frequency VLBI data are available, we apply the same upward projection to ν_0 with $\alpha = -0.5$. For non-detections, we adopt a 3σ upper limit, where σ is the image RMS. VLBI images often resolve multiple components with separations exceeding the synthesized beam of our ν_0 measurements; to remain conservative for an upper-limit estimate, we treat the central emission as an extended-jet and sum the flux densities of all components before projection. If the VLBI-based projection is smaller than the low-frequency extended-jet estimate from archival data, it is adopted. Note that VLBI extrapolations of the sample are not extensive. Additional VLBI studies not included in this paper include NGC 1068 (Muxlow et al. 1996; Gallimore et al. 2004; Fischer et al. 2023; Gallimore & Impellizzeri 2023; Mutie et al. 2024, 2025); NGC 3079 (Middelberg et al. 2003);

⁵ Extended-jet refers to emission originating beyond the compact, self-absorbed jet base associated with the AGN and strong-gravity regime.

Circinus (Prieto et al. 2004); and NGC 4945 (Lenc & Tingay 2009).

3.5. Variability Analysis

Variability provides valuable physical insight into the emission mechanisms at play. Detected variability serves as a diagnostic that rules out thermal-dust or star-formation emission as the dominant contributor, since such thermal processes remain stable on human timescales (Kennicutt & Evans 2012; Murphy et al. 2011). In contrast, variability in AGN is a key signature of SMBH activity, with characteristic timescales often modeled as $\propto M_{\text{BH}}/\dot{m}$ (Bower et al. 2015; Chen et al. 2023). Variability is not, however, uniquely indicative of AGN processes, as it can also arise from jets (Lister et al. 2009; Hovatta et al. 2007), circumnuclear variations (e.g., absorption, turbulence, winds, or photoionized gas), and transient or extrinsic phenomena such as TDEs, blazar flares, and microlensing (Cackett et al. 2021; Gezari 2021). Due to degenerative physical models in the variability modeling landscape, we do not go so far as to attribute variability to strong evidence of AGN activity.

The reason we analyze variability in this work is primarily to obtain upper limits of systematic uncertainties for extended-jet and submm-mm AGN emission. No variability estimates are applied to thermal-dust extrapolations, as dust emission remains stable on human timescales. We characterize variability in two frequency regimes – above and below 200 GHz – to separately constrain AGN and extended-jet behavior. Frequency mismatch and image noise are considered when deriving upper limits on variability⁶, as illustrated in the Variability Plots of Section 4. Upper limits from these plots are adopted in the Continuum Flux and Extrapolation Tables of Section 4 to ensure conservative flux uncertainty estimates for extended-jet extrapolations and ν_0 measurements.

If variability estimates are not available for the lower-frequency regime, they are not reported for extended-jet systematic errors in brightness. Likewise, if variability estimates are not available for the upper-frequency regime, they are not reported for ν_0 systematic errors in brightness.

When variability estimates are available for the lower-frequency regime but not for the higher-frequency regime, the systematic uncertainty for the extended-jet extrapolations adopts variability estimates corresponding to the $\alpha = 0$ upper limit, since the difference between

$\alpha = -0.5$ and $\alpha = 0$ extrapolations is negligible for our analysis. When variability estimates are available for the higher-frequency regime but not for the lower-frequency regime, the systematic uncertainty for the ν_0 measurements adopts the variability estimates corresponding to the $\alpha = +2.5$ ⁷ upper limits in the higher-frequency regime; otherwise, no systematic uncertainty is provided (Kellermann & Pauliny-Toth 1981).

When variability estimates are available for both frequency regimes, the systematic flux uncertainty of the ν_0 measurements is computed as a linearly brightness-weighted average, adopting variability estimates corresponding to the optically thick synchrotron upper limit ($\alpha = +2.5$) in both regimes to ensure internal consistency. The weight factor for variability in the lower-frequency regime is defined as the ratio of the ν_0 flux to the sum of the ν_0 flux and the non-extrapolated measurement of the flux chosen for the extended-jet extrapolation. Similarly, the weight factor for variability in the upper-frequency regime is defined as the ratio of the thermal-dust flux to the same total.

To quantify variability, we adopt a statistical approach tailored to our heterogeneous dataset, which combines observations from different instruments, epochs, and beam-sizes across the submm-mm regime. Because repeated measurements at identical frequencies and resolutions are unavailable, we identify pairs of observations that are closely matched in frequency and beam-size to estimate variability while minimizing spectral and spatial biases. Although we do not explicitly account for mismatched bandwidth or frequency coverage in this work, our filtering of observation pairs preserves the comparability of the relevant telescope parameters to the extent possible.

We restrict variability analysis to observation pairs closely matched in both frequency ($|\nu_2 - \nu_1|/\langle \nu \rangle < 0.014$) and beam-size (within $|\theta_2 - \theta_1|/\langle \theta \rangle < 0.026$); where $\nu_{1,2}$ and $\theta_{1,2}$ represent the frequency and FWHM-beam-size values for the pair of observation points. These thresholds were chosen empirically to maximize pair counts while minimizing spectral and beam-related biases. These quantities are organized into a symmetric rank-2 tensor to express all pairwise comparisons, with the resulting filtered data provided in Table 4.

For each observational pair in Table 4, we compute the flux difference, $|S_1 - S_2|/\langle S \rangle$, where S_1 and S_2 represent the flux densities of the paired observations. By propagating the errors of the flux estimates found in Table 3, the uncertainty in the flux difference is adopted

⁶ Beam-size mismatch is not considered due to the sparse sampling of time and beam-size in our dataset (See Section 5).

⁷ We use $\alpha = +2.5$ as the spectral index for optically thick AGN.

(this is referred to as the $\alpha=0$ uncertainty). Using this value of uncertainty, only points with a significance of the flux difference greater than 3 are retained.

If both measurements in a pair correspond to non-detections, the pair is discarded. A pair is also discarded if the non-detection value exceeds the detected flux. When the non-detection flux lies below the detected flux, we treat the pair as a lower limit on the flux difference. In this case, the flux difference is obtained by taking the detected flux and adding the image noise to it ($S_1 \rightarrow S_1 + \Delta S_1$) while computing the flux difference.

Variability plots for each source are shown in the Figures of Section 4. Points are grouped by frequency below and above 200 GHz. The percent difference in flux density is plotted on the vertical axis, the time difference on the horizontal axis, and the frequency is encoded by color. Horizontal lines spanning the x-axis indicate the upper limits on variability for the two frequency regimes, both with and without applying frequency corrections. These limits are used as the systematic uncertainties reported in the Tables of Section 4.

To incorporate frequency-mismatch into variability upper-bound estimates, we consider an optically thick AGN ($\alpha = +2.5$) and extended-jet ($\alpha = -0.5$) behavior. We model $S_\nu \propto \nu^\alpha$ to obtain the α dependence on percent flux difference:

$$\frac{S_1 - S_2}{\langle S \rangle}(\alpha) = 2 \frac{1 - (\nu_2/\nu_1)^\alpha}{1 + (\nu_2/\nu_1)^\alpha}. \quad (5)$$

The maximum flux difference percentage under our constraint filter is obtained at the largest allowed frequency offset, ($|\nu_2 - \nu_1|/\langle \nu \rangle < 0.014$). For extended-jet-induced spectral energy density (SED) variation ($\alpha = -0.5$), this value is $< 0.1\%$, negligible relative to estimates without spectral corrections (often $\sim 10\%$). Therefore, when low-frequency variability estimates are available, we adopt the upper limit from $\alpha = 0$ in the Variability Plots for simplicity. On the other hand, if we consider an unresolved variable emission with $\alpha = +2.5$, we find the maximum flux difference percentage to be $\sim 3.9\%$. The contribution of frequency mismatch to variability in the submm-mm regime is, therefore, significant and is incorporated into the systematic uncertainty in submm-mm AGN-core flux estimates by adding the frequency mismatch term with its appropriate sign to the $\alpha = +2.5$ uncertainty.

4. INDIVIDUAL SOURCE DISCUSSION

Each source subsection includes the predicted BHS size, SED, AGN-core brightness at the reference frequency with thermal-dust/extended-jet contamination estimates and variability diagnostics, and a review of mass and inclination precisions from water maser modeling. We also describe the 22 GHz water maser spectrum, and higher-frequency water maser lines when relevant, before concluding with source-specific context.

4.1. NGC 4258

NGC 4258 exhibits the largest angular BHS among the known water maser sources, with an estimated diameter of $0.617 \pm 0.049 \mu\text{as}$, as shown in Table 2. A baseline between Earth and L2 yields a fringe spacing ≈ 3.4 times finer than the BHS diameter of NGC 4258. Proposed missions such as *Origins* and *Millimetron* could provide this baseline with sufficient sensitivity to image the BHS; however, achieving full image reconstruction will require further research into how to fill the (u, v) plane.

While numerous archival observations exist for this source in the VLA database, its northern declination places it outside ALMA’s observing range. As a result, no ALMA archival data are available above 43 GHz. Nonetheless, we present three continuum measurements above this frequency obtained from the SMA, SCUBA-JCMT, and NMA.

The SED of NGC 4258, shown in Figure 2, exhibits a general trend of increasing brightness with frequency from ~ 40 -320 GHz, which we attribute to advection dominated accretion flow (ADAF)-driven AGN emission. Measurements of the continuum flux and the spectral index α for this image from the SMA observations on January 31, 2022, and March 16, 2023, are not in agreement (Table 1). The difference in continuum flux can be attributed to intrinsic variability, consistent with behavior observed at lower frequencies. It may also arise from mismatched beam-sizes and extended emission, or from the characteristic shape of the SED in the submillimeter-millimeter regime. On the other hand, the discrepancy in α , shifting from 4.7 to 1.1 over a frequency change of only 10 GHz, is difficult to explain using any plausible physical mechanism. We suggest that this extrapolation of α is likely inconsistent due to statistical error, and we propose that obtaining a more reliable value of α will require additional observations of this source with the SMA (See Section 5). We adopt $\alpha = 2.9 \pm 2.1$ as the statistical average between the two measurements. Although this value provides only a very

Table 1. Spectral Index Extrapolation for SMA Observations

Source	LSB Flux	USB Flux	Extrapolated α
NGC 4258 ¹	8.5 ± 1.0	13.0 ± 0.7	4.7 ± 1.4
NGC 4258 ²	6.3 ± 0.7	6.9 ± 0.7	1.1 ± 1.6
NGC 3079 ¹	34.0 ± 0.4	43.8 ± 0.4	2.88 ± 0.17
NGC 1068 ¹	54.0 ± 0.1	46.3 ± 0.1	-1.73 ± 0.04

NOTE— Extrapolation of the Spectral Index α from SMA observations presented in this paper. Superscript¹ refers to the observation on March 16, 2023 with upper and lower side band of 215.6, 235.6 GHz. Superscript² refers to the observation on Jan 31, 2022 with upper and lower side band of 225.6, 245.6 GHz

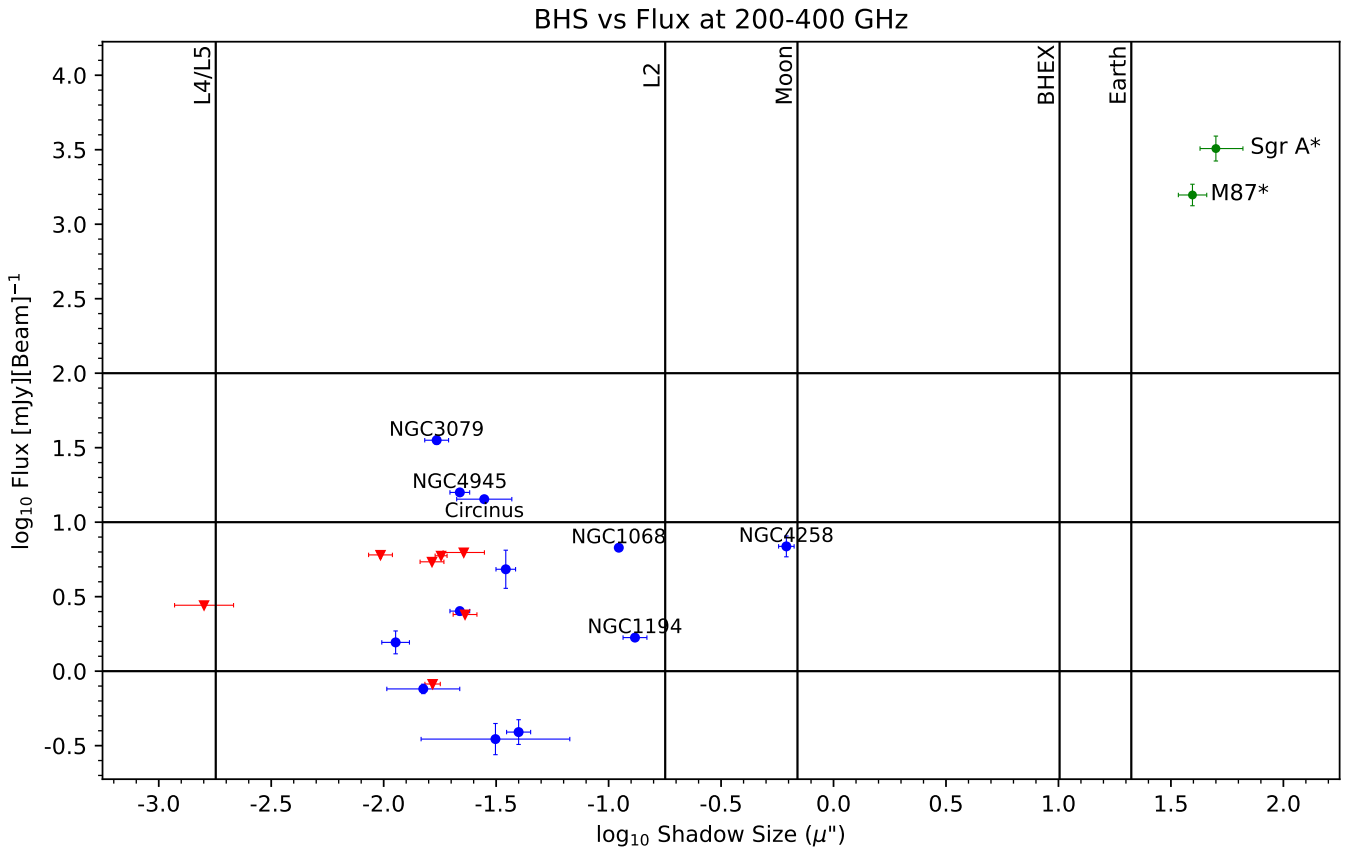


Figure 1. Resolution and sensitivity requirements for resolving BHS of water megamaser SMBHs using VLBI. Each point shows an approximate estimate of angular BHS size and flux density at submm-mm for a given water megamaser AGN. ● symbols represent detections, and ▼ symbols represent upper limits. ● symbols represent M87, Sgr A* for comparison. Vertical lines correspond to the angular resolution at 230 GHz for baselines equal to (1) the Earth diameter, (2) Earth–Moon, (3) Earth–L2, and (4) Earth–L4/L5 distances. Horizontal lines mark representative VLBI sensitivity thresholds.

Table 2. Angular Size, Mass, Distance, and Inclination for the Sample of SMBH-Hosting Galaxies

Source	$\theta_{\text{BHS}} [\mu\text{as}]$	$\log_{10}(M_{\bullet}/M_{\odot})$	$D [\text{Mpc}]$	$i [{}^{\circ}]$
Sgr A*	¹ 51.8 ± 2.3	⁵ 6.633 ± 0.0012	¹ 0.00815 ± 0.00015	³ ≤ 30
M87*	² 42 ± 3	⁶ 9.74 ± 0.03	² 16.8 ± 0.8	⁴ ~ 17
NGC 4258	0.617 ± 0.049	⁷ 7.58 ± 0.03	¹⁵ 6.32 ± 0.26	¹⁴ 87.05 ± 0.09
NGC 1194	0.131 ± 0.016	⁷ 7.85 ± 0.05	¹⁵ 55.3 ± 2.2	⁸ 85
NGC 1068	0.111 ± 0.005	¹⁰ 7.22 ± 0.003	¹⁸ 15.4 ± 0.6	⁸ 90
NGC 5765b	0.0398 ± 0.0049	⁷ 7.64 ± 0.05	¹⁵ 113 ± 5	¹¹ 72.4 ± 0.5
NGC 2273	0.0349 ± 0.0035	⁷ 6.93 ± 0.04	¹⁵ 25.0 ± 1.0	⁸ 84
NGC 3393	0.0314 ± 0.0239	⁷ 7.20 ± 0.33	²¹ 51.9 ± 2.1	⁸ 90
Circinus	0.0280 ± 0.0079	⁷ 6.06 ± 0.10	²⁰ 4.207 ± 0.698	⁸ 90
CGCG 074-064	0.0265 ± 0.0026	⁹ 7.384 ± 0.038	¹⁷ 93.6 ± 3.8	⁹ 90.8 ± 1.7
NGC 6264	0.0230 ± 0.0028	⁷ 7.49 ± 0.05	¹⁵ 138 ± 6	¹¹ 91.3 ± 2.3
UGC 3789	0.0227 ± 0.0048	⁷ 6.99 ± 0.09	¹⁵ 44.1 ± 1.8	¹¹ 84.9 ± 0.6
NGC 4388	0.0218 ± 0.0022	⁷ 6.86 ± 0.04	²² 34.2 ± 1.4	⁸ 90 ± 0
NGC 4945	0.0186 ± 0.0077	⁸ 6.14 ± 0.18	¹⁹ 7.6 ± 0.3	⁸ 90
UGC 6093	0.0180 ± 0.0011	⁷ 7.41 ± 0.02	¹⁷ 146 ± 6	¹³ 93.84 ± 3.94
NGC 3079	0.0172 ± 0.0021	⁷ 6.40 ± 0.05	²⁴ 15.0 ± 0.6	⁸ 84
ESO 558-G009	0.0165 ± 0.0013	⁷ 7.22 ± 0.03	¹⁵ 103 ± 4	¹² 98 ± 1
NGC 2960	0.0164 ± 0.0020	⁷ 7.03 ± 0.05	¹⁵ 67.0 ± 2.7	⁸ 89
J0437+2456	0.0157 ± 0.0023	⁷ 7.00 ± 0.06	¹⁵ 65.2 ± 2.7	¹² 81 ± 1
NGC 1320	0.0150 ± 0.0056	⁷ 6.74 ± 0.16	²³ 37.7 ± 1.5	⁸ 90 ± 0
IC 2560	0.0113 ± 0.0016	⁷ 6.64 ± 0.06	¹⁶ 39.6 ± 1.6	⁸ 90
NGC 6323	0.00968 ± 0.00118	⁷ 7.00 ± 0.05	¹⁵ 106 ± 4	¹¹ 91.5 ± 0.3
Mrk 1029	0.00159 ± 0.00048	⁷ 6.28 ± 0.13	²⁵ 123 ± 5	¹² 79 ± 2

NOTE— This is a sample of the 20 best known SMBH-Hosting Galaxies supplemented by Sgr A* and M87* for comparison. Logarithmic and linear errors have been symmetrized.

— The superscript reference codes correspond to the following categories: ^{1–4} refer to results from the EHTC's studies of Sgr A* and M87; ^{5,6} indicate mass measurements based on dynamical estimators for Sgr A* and M87; ^{7–14} include mass and inclination angle measurements obtained via water maser observations; ^{15–25} indicate distance measurements, with corresponding ADS bibcodes listed below. Specifically, ^{15,16} are distances derived from maser measurements.

References— ¹ Event Horizon Telescope Collaboration et al. (2022d); ² Event Horizon Telescope Collaboration et al. (2019f); ³ Event Horizon Telescope Collaboration et al. (2022f); ⁴ Event Horizon Telescope Collaboration et al. (2021b); ⁵ GRAVITY Collaboration et al. (2022); ⁶ Simon et al. (2024); ⁷ Greene et al. (2016); ⁸ Zhang et al. (2024); ⁹ Pesce et al. (2020a); ¹⁰ Gallimore et al. (2024); ¹¹ Pesce et al. (2020b); ¹² Gao et al. (2016b); ¹³ Zhao et al. (2018); ¹⁴ Reid et al. (2019); ¹⁵ 2018ApJ...863..149P Pesce et al. (2018); ¹⁶ 2015ApJ...810...65P Pesce et al. (2015); ¹⁷ 2016SDSSD.C...0000: Albareti et al. (2017); ¹⁸ 2024ApJ...964..172B Baer-Way et al. (2024); ¹⁹ 2023MNRAS.519.6184K Kanehisa et al. (2023); ²⁰ 2009AJ....138..323T Tully et al. (2009); ²¹ 2022ApJS..261....6K Koss et al. (2022); ²² 1993ApJS...88..383L Lu et al. (1993); ²³ 2017A&A...599A.104T Theureau et al. (2017); ²⁴ 2005ApJS..160..149S Springob et al. (2005); ²⁵ 1999ApJS..121..287H Huchra et al. (1999).

Table 3. Continuum Brightness Parameters: Machine Readable Table 1

[1]	[2]	[3]	[4]	[5]	[6]	[7]	[8]
Circinus	ALMA	86	22.8	2016/07/02_1	1.38	51	member.uid ... pbcor.fits
Circinus	ALMA	93	42.2	2016/01/14_1	2.64	178	member.uid ... pbcor.fits
Circinus	ALMA	108	40.5	2014/12/27_1	2.40	137	member.uid ... pbcor.fits
Circinus	ALMA	108	39.8	2016/03/18_1	1.54	159	member.uid ... pbcor.fits
Circinus	ALMA	178	27.2	2021/06/14_1	0.245	278	member.uid ... pbcor.fits
Circinus	ALMA	178	16.6	2021/08/20_1	0.0535	517	member.uid ... pbcor.fits
Circinus	ALMA	182	22.6	2018/12/01_1	0.597	43	member.uid ... pbcor.fits
Circinus	ALMA	186	19.0	2023/12/05_1	0.210	184	member.uid ... pbcor.fits
Circinus	ALMA	223	50.5	2019/05/05_1	5.83	36	member.uid ... pbcor.fits
Circinus	ALMA	225	54.9	2019/01/18_1	5.98	13	member.uid ... pbcor.fits

NOTE— [1]: Source Name [2]: Frequency [GHz] [3]: Telescope [4]: Flux [mJy beam^{-1}] [5]: Date [YYYY-MM-DD_x] [6]: Beam Size FWHM [arcsec] [7]: SNR [8]: Filename

First 10 lines of the machine-readable table containing the parameters of the Gaussian fits. The size and position angle of each Gaussian are fixed to match the synthesized beam, and the centroid position is fixed to the fit of the gaussian ν_0 , outlined in Section 2.4. Flux densities marked with an asterisk (*) denote non-detections. If the number following the underscore in the date (i.e., the value x in column [5]) is not 1, it denotes an additional observation taken for the same source, at the same frequency, on the same date.

Table 4. Variability of Continuum Brightness Parameters: Machine Readable Table 2

[1]	[2]	[3]	[4]	[5]	[6]	[7]	[8]	[9]	[10]	[11]	[12]	[13]
Circinus	223	223	[1.0]	5.83	5.98	[2.5]	50.5	54.9	[8.3±8.0]	2019/06/21	2019/06/29	[0.023]
Circinus	223	223	[1.0]	5.83	5.92	[1.5]	50.5	52.7	[4.2±7.9]	2019/06/21	2019/06/30	[0.026]
Circinus	225	225	[<1]	5.98	5.92	[<1]	54.9	52.7	[4.1±10.6]	2019/06/29	2019/06/30	[0.003]
Circinus	318	318	[<1]	0.261	0.257	[1.6]	31.4	28.6	[9.3±4.2]	2022/01/27	2017/06/31	[4.574]
IC2560	22	22	[<1]	3.66	3.66	[<1]	17.1	17.1	[<1]	1998/02/31	1998/03/01	[0.003]
NGC1068	1.4	1.4	[1.4]	16.1	16.5	[2.5]	3931.7	2322.0	[51.5±5.3]	1992/12/08	1983/09/09	[9.248]
NGC1068	4.9	4.9	[<1]	14.1	14.3	[1.3]	2018.3	1340.7	[40.3±9.8]	2003/08/18	1983/10/07	[19.865]
NGC1068	223	223	[1.3]	5.90	5.88	[<1]	49.5	50.3	[1.6±13.3]	2022/08/21	2023/08/09	[0.968]
NGC1068	226	226	[<1]	5.88	5.81	[1.1]	50.3	46.8	[7.1±13.3]	2023/08/09	2022/10/10	[0.831]
NGC1068	265	265	[<1]	0.140	0.143	[2.3]	10.4	8.6	[18.5±3.1]	2016/03/09	2016/03/09	[0.000]

NOTE— [1]: Source Name [2]: Frequency 1 [GHz] [3]: Frequency 2 [GHz] [4]: Frequency Difference [%] [5]: Beam Size 1 FWHM [arcsec] [6]: Beam Size 2 FWHM [arcsec] [7]: Beam Size Difference [%] [8]: Flux 1 [mJy beam^{-1}] [9]: Flux 2 [mJy beam^{-1}] [10]: Flux Difference [%] [11]: Date 1 [YYYY-MM-DD] [12]: Date 2 [YYYY-MM-DD] [13]: Time Difference [yrs]

First 10 lines of the machine-readable table provide pairwise comparisons between observations of each source. For every observation pair, the table lists the differences in flux density, observing frequency, beam size, and observation date. This table only presents observation pairs with relative differences in frequency below 1.4 % and relative differences in beam size below 2.6%.

loose constraint, it remains consistent with the SED expected from an ADAF.

Below 40 GHz, the SED shape is difficult to constrain due to sparse sampling in beam-size and frequency, as well as limited characterization of variability. As demonstrated in Figure 2, the source is indeed variable at extended-jet-dominated frequencies, consistent with multi-epoch VLBI studies (Herrnstein et al. 1998b).

Thermal-dust contamination indicates that it cannot be the dominant emission process in the submm to mm regime. Extended-jet contamination is also negligible, even when considering variability constraints. We note that no variability constraints were formally established for the submm-mm regime. Overall, we suggest that the emission in the submm-mm regime arises from an ADAF-AGN.

22 GHz water masers in this source trace a thin Keplerian disk at radii ranging from 0.11 ± 0.004 to 0.29 ± 0.01 pc from the SMBH (Gao et al. 2016b; Humphreys et al. 2008). The disk is also warped: the inclination varies from 84 to 92 degrees on the red- and blue-sided portions of the disk. No search for water masers other than 22 GHz has been conducted for this source. 22 GHz water maser measurements constrain the BH mass to $\sim 7\%$ and the (edge-on) disk inclination to $\sim 0.1\%$ (Table 2).

A baseline between Earth and the Moon is not sufficient to resolve the BHS of NGC 4258 but it is adequate to search for the BHS-megamaser disk dynamical-center offset, provided that astrometric precision for the water maser dynamical center improves by a factor of ~ 55 to reach the required $\sigma_\theta \lesssim 0.09\mu\text{as}$ (see Section 3.3). It is possible that missions such as *LOVEX* could provide such a baseline; however, their receiving frequencies would need to accommodate 230 GHz. Moreover, unless submm-mm water maser emissions can be identified in this source, this would require simultaneous cross-band imaging and calibration at 22 and 230 GHz.

Lasota et al. (1996) used the ADAF model to predict a ~ 5 mJy flux density at 22 GHz for NGC 4258 (see Herrnstein 1998a). In 1998, a continuum image at 22 GHz resolved extended-jet components above and below the position of the SMBH, but no central component was detected, establishing an upper limit of 0.220 mJy within an effective spatial resolution of 0.014 pc (Herrnstein et al. 1998b). To explain this discrepancy with the ADAF-based prediction, Herrnstein et al. (2005) proposed two scenarios: (1) the source hosts no ADAF and instead accretes through a mass-starved thin disk that extends to the innermost stable circular orbit, or (2) the disk remains thin down to some transition ra-

dius ($< 100 R_S$), interior to which it transforms into an ADAF. In the second case, the power spectrum rise predicted by Mahadevan (1997) would occur at frequencies above 22 GHz.

The results presented in this paper show submm-mm excess, consistent with ADAF model predictions and supportive of Herrnstein’s second scenario. Additional evidence for ADAF activity in NGC 4258 includes the presence of twisted nuclear jets observed at radio, optical, and X-ray wavelengths, which may be explained by magnetically driven bipolar outflows near the axis of a quasi-spherical inflow. Furthermore, the observed X-ray and optical/UV luminosities are well below the Eddington limit (Narayan & Yi 1995), consistent with a radiatively inefficient accretion flow.

If NGC 4258 indeed hosts an ADAF-type accretion flow, as has been proposed for M87* and Sgr A*, then characterizing its spectrum would allow for the identification of the turnover frequency marking the transition from optically thick to optically thin synchrotron emission, thereby enabling probes of photon-ring substructure.

4.2. NGC 1194

Among the sources considered, NGC 1194 exhibits the second-largest predicted BHS, with a size of $0.131 \pm 0.049 \mu\text{as}$ shown in Table 2. Its relatively large BHS size is attributable to its high BH mass, although the host AGN is significantly more distant than the other sources in the selected sample, located at 55 Mpc from Earth. NGC 1194 is the only source in the sample situated beyond 30 Mpc, making it a potential candidate for incorporating higher-order gravitational redshift corrections (Villaraos et al. 2022). 22 GHz water maser measurements constrain the BH mass with a precision of approximately 10% and determine the disk inclination angle to 85° . A SVLBI mission to provide fringe spacing comparable to BHS-scale features would require a baseline 1.4 times longer than the Earth-L2 separation and would need to achieve a brightness sensitivity of ~ 2 mJy at 230 GHz.

Despite its favorable angular diameter, NGC 1194 exhibits notably faint radio emission, a property that may be partly attributable to its relatively large distance from Earth compared to the rest of the sample. The low flux density of NGC 1194 at 229 GHz presents a significant limitation for future efforts to resolve its event horizon. The AGN-core brightness is estimated to be only ~ 2 mJy beam $^{-1}$ at 229 GHz (Table 6). Extended-jet emission could not be ruled out through low-frequency

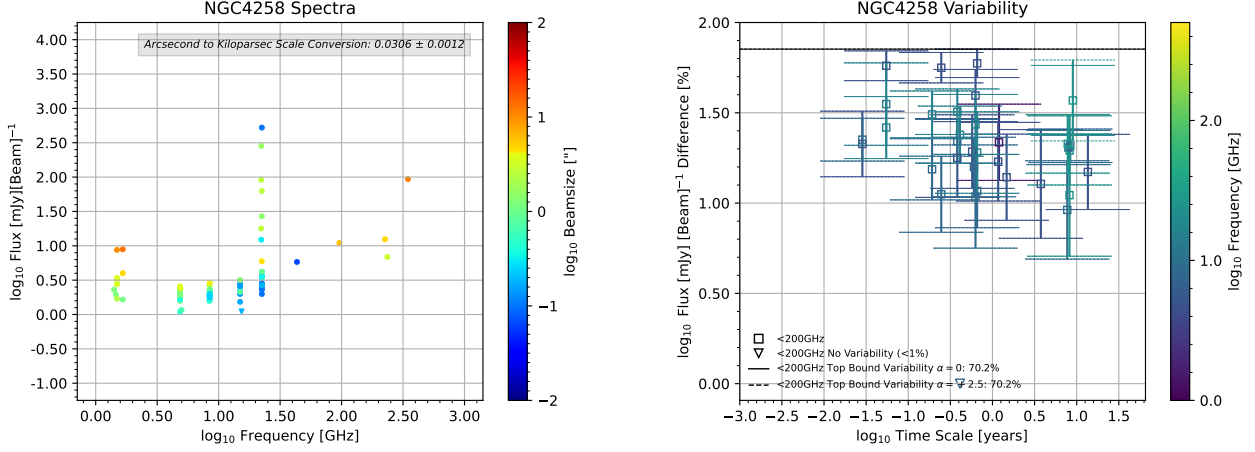


Figure 2. Left Panel: SED of NGC 4258. Data points correspond to continuum observations from the SMA, SCUBA-JCMT, VLA, and NMA. Due to its northern declination, NGC 4258 is outside the observable range of ALMA. The inset shows the angular to linear scale, and the color bar denotes FWHM synthesized beam size. Right Panel: Variability of NGC 4258. The horizontal axis indicates the time difference between observations, while the vertical axis shows the percentage difference in flux density between the two observations.

Table 5. Continuum Flux and Extrapolation to 226 GHz for NGC 4258

Source	Emission	Telescope	Flux[mJy[beam] $^{-1}$]	Frequency[GHz]	beamsize["]	Date[yyyy/mm/dd]
NGC 4258	ν_0	SMA	6.9 ± 1.1	236	3.32	2022/01/31
NGC 4258	Thermal-Dust	SCUBA-JCMT	0.8 ± 0.3	347	15.00	NA
NGC 4258	Extended-Jet	VLA	$0.14^{+0.2}_{-0.1} \pm 0.02$	1.5	2.43	1997/01/07

NOTE— ν_0 The observation with the smallest beam size between 200–400 GHz. High Dust Extrapolation: The lowest extrapolated value of thermal-dust is reported. Low Jet Extrapolation: The lowest extrapolated value of extended-jet is reported. VLBI observations from (Herrnstein et al. 1998b) are considered as well. We report two uncertainties: the first accounts for source variability (multiplicative factor 2.08) and the second for image noise.

extrapolation, and the lack of high-frequency imaging leaves open the possibility that the observed flux arises from thermal-dust. Nonetheless, as shown in Figure 3, the spectrum looks flat from ~ 5 –250 GHz, which is often interpreted as arising from an AGN-core (Blandford & Königl 1979; Shabala et al. 2012).

22 GHz water masers in this source trace a Keplerian disk at radii ranging from $0.54^{+0.25}_{-0.03}$ to $1.33^{+0.06}_{-0.97}$ pc from the SMBH (Gao et al. 2016b). In addition to this well-characterized 22 GHz emission, the source also exhibits 183 GHz water masers, although they are significantly fainter than the ~ 1 Jy counterparts at 22 GHz (Pesce et al. 2023). The 183 GHz water masers are most prominent near the systemic velocity and closely correspond to the systemic features of the 22 GHz water masers.

4.3. NGC 3079

Although the SMBH in this source is the smallest among the primary targets – exhibiting a BHS size of $0.0172 \pm 0.0021 \mu\text{as}$, as shown in Table 2 – it is also the brightest at 230 GHz. 22 GHz water maser measurements constrain the BH mass with a precision of approximately 10% and determine the disk inclination angle to 90° . A SVLBI mission to provide fringe spacing comparable to BHS-scale features would require a baseline 10.5 times longer than the Earth-L2 separation and would need to achieve a brightness sensitivity of ~ 36 mJy at 230 GHz.

Although numerous archival observations are available in the VLA database, the source’s northern declination places it outside ALMA’s observing range. Consequently, no ALMA archival data exist above 43 GHz. For frequencies beyond this threshold, we include only

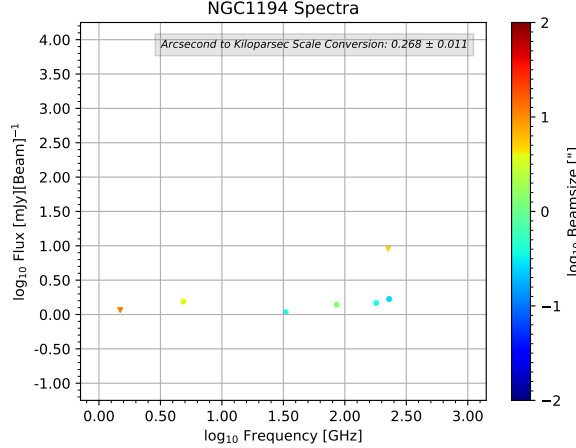


Figure 3. SED of NGC 1194. Data points correspond to continuum observations from the SMA, ALMA, and VLA. The inset shows the angular to linear scale, and the color bar denotes FWHM synthesized beam size.

Table 6. Continuum Flux and Extrapolation to 229 GHz for NGC 1194

Source	Emission	Telescope	Flux[mJy[beam] $^{-1}$]	Frequency[GHz]	beamsize["]	Date[yyyy/mm/dd]
NGC 1194	ν_0	ALMA	1.7 ± 0.1	229	0.21	2016/10/24
NGC 1194	Extended-Jet	VLA	0.094 ± 0.04	1.5	14.88	1988/05/03

NOTE— ν_0 : The observation with the smallest beam size between 200–400 GHz. High Dust Extrapolation: Not applicable for this source, as no high frequency observations are available. Low Jet Extrapolation: The lowest extrapolated value of extended-jet is reported.

the SMA observation presented in this work. The SED of NGC 3079 is shown in Figure 4. The spectrum appears to decline from \sim 1–30 GHz, reaching a peculiar minimum brightness of \sim 3 mJy beam $^{-1}$ in the VLA observation at 43 GHz.

As shown in Table 7, the 226 GHz SMA observation presented in this paper measures a peak flux density of \sim 36 mJy beam $^{-1}$. While extended-jet emission contamination is negligible, the lack of high-frequency imaging leaves open the possibility that the observed flux arises from thermal-dust.

The extrapolated spectral index α in Table 1 indicates a rising spectrum that may align with expectations for an optically thick ADAF region, consistent with the comparison of the 43 GHz to 226 GHz observations. Yet, as demonstrated by the inconsistent α values reported for NGC 4258, the index is strongly affected by dataset-dependent variation that is not captured by the formal uncertainties.

22 GHz water masers in this source trace a Keplerian disk at radii ranging from 0.4 to 1.3 pc from the SMBH (Humphreys et al. 2005). In addition to 22 GHz,

NGC 3079 exhibits water maser transitions at 183 GHz and 439 GHz. The 183 GHz components occur within the same velocity range as the 22 GHz components, suggesting that both transitions may originate from the same physical regions, typically associated with the disk and, in some cases, the outflow. On the other hand, the 439 GHz components may originate from gas located closer to the SMBH than the bulk of the 22 GHz components, as 439 GHz water maser components are predicted to be pumped within a narrower range of higher temperatures and densities than those required for 22 GHz emission.

The water maser components in this source exhibit: (1) significant structure orthogonal to the general elongation, (2) large velocity dispersion in compact regions on the sky, and (3) a flat rotation curve. Accretion onto the BH drives a jet that is misaligned with the disk rotation axis and interacts with a dense ambient medium (Kondratko et al. 2005). These features seem parallel to those observed in NGC 1068 (Gallimore et al. 2024), where a model has been adopted in which the water masers trace spiral arms and are offset from the disk

midline due to a disk wind lifting the corresponding clouds.

4.4. NGC 4945

The size of the BHS for this source is estimated to be $0.0186 \pm 0.0077 \mu\text{as}$. 22 GHz water maser measurements constrain the BH mass with a precision of approximately 40% and determine the disk inclination angle to 90° (Table 2). A SVLBI mission to provide fringe spacing comparable to BHS-scale features would require a baseline 9.5 times longer than the Earth-L2 separation and would need to achieve a brightness sensitivity of $\sim 16 \text{ mJy}$ at 230 GHz.

While numerous archival observations exist for this source in the ALMA database, its southern declination places it outside the observing range of the SMA and VLA. Consequently, no archival data are available below 86 GHz. The SED of NGC 4945 is shown in Figure 5. The limited beam-size information for this source makes it difficult to identify clear trends in the data; nevertheless, we are able to probe variability in the 200-400 GHz range (Figure 5).

As shown in Table 8, the 349 GHz ALMA observation presented in this paper measures a peak flux density of $\sim 16 \text{ mJy beam}^{-1}$. The thermal-dust extrapolation contamination is negligible. At centimeter wavelengths, the emission is dominated by star formation, such that free-free radiation provides the dominant contribution (Emig et al. 2020; Bendo et al. 2016), which is consistent with the host's high visual extinction (Moorwood et al. 1996; Goulding & Alexander 2009). Therefore, although the extended-jet extrapolation method presented here suggests a contribution of $\sim 28 \text{ mJy beam}^{-1}$, this interpretation is not adopted.

The primary indication of AGN activity comes from its variable hard X-ray emission; in fact, NGC 4945 is among the brightest sources in the X-ray sky (Emig et al. 2020). The X-ray luminosity is highly variable, with a timescale of ~ 1 day (Hagiwara et al. 2021). It is also one of the nearest galaxies known to host both an AGN and active starburst regions in coexistence (Pérez-Beaupuits et al. 2011; Marconi et al. 2000).

Variability in the 321 GHz continuum emission for this source has been observed to correlate with the water maser components, and it has been suggested that this variability originates from X-ray emission. Accordingly, we propose that the ν_0 submm-mm emission may also be attributed to an AGN-core (Figure 5).

Fabian et al. (1998) proposed that, for this source, mechanical energy from supernovae and stellar winds pre-

vents interstellar clouds from collapsing into a thin disk, thereby sustaining star-forming regions on minor orbits that obscure most lines of sight to the active nucleus (Marconi et al. 2000). Consistent with this interpretation, Spoon et al. (2003) used mid-infrared spectra of NGC 4945 to reveal an extended, fragmented, and vigorously star-forming rotating molecular ring or disk that surrounds a deeply buried AGN.

22 GHz water masers in this source trace a Keplerian disk within ~ 0.3 pc from the SMBH (Greenhill et al. 1997). While the angular distribution of blue-shifted components is roughly linear, the red-shifted components do not mirror the structure of their blue-shifted counterparts, and the positional errors of individual water maser components are substantial. Furthermore, the low declination of the source limited the range of observed hour angles, resulting in phase measurements with significant statistical errors. For these reasons, the mass measurement for the source provided is not well constrained.

In addition to the well-known 22 GHz water maser emission, NGC 4945 has also been observed to exhibit water maser transitions at 183 GHz and 321 GHz (Humphreys et al. 2016; Hagiwara et al. 2021; Pesce et al. 2016). The 321 GHz components do not map one-to-one with the velocities of the 22 GHz emission. Rather, and quite intriguingly, the 321 GHz peaks fall precisely where the 22 GHz emission drops off. Since 321 GHz water masers have a higher optimal kinetic temperature, they may originate in the accretion disk at radii interior to those traced by the 22 GHz emission.

4.5. Circinus

The size of the BHS for this source is estimated to be $0.0280 \pm 0.0079 \mu\text{as}$ (Table 2). 22 GHz water maser measurements constrain the BH mass with a precision of approximately 23%, significantly less certain than the rest of the sample (excluding NGC 4945), and determine the disk inclination angle to 90° . A SVLBI mission to provide fringe spacing comparable to BHS-scale features would require a baseline 6.4 times longer than the Earth-L2 separation and would need to achieve a brightness sensitivity of $\sim 14 \text{ mJy}$ at 230 GHz.

While numerous archival observations exist for this source in the ALMA database, its southern declination places it outside the observing range of the SMA and VLA. As a result, no archival data are available below 86 GHz. It is also worth noting that this source lies close to the plane of the Milky Way, adding complications such as scintillation and high galactic ex-

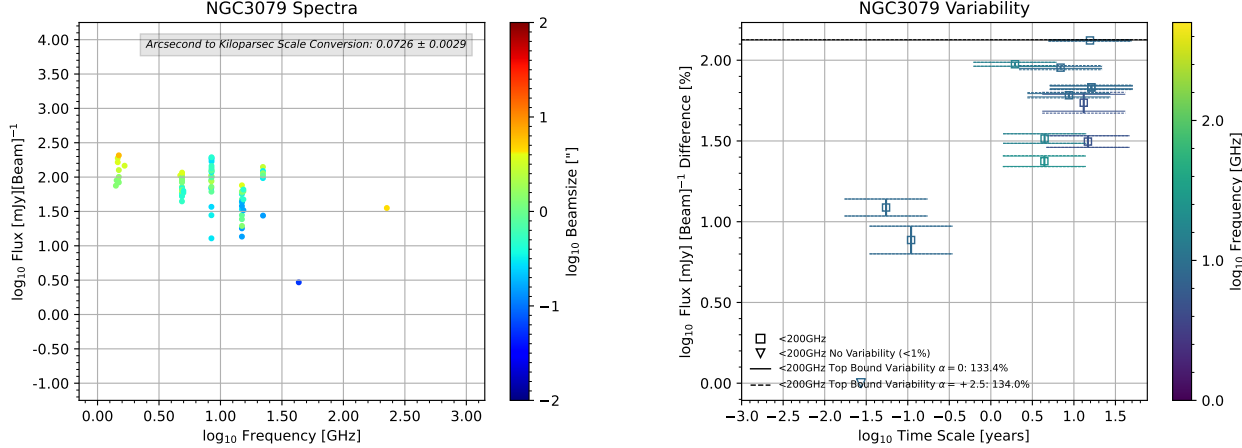


Figure 4. Left Panel: SED of NGC 3079. Data points correspond to continuum observations from the SMA and VLA. Due to its northern declination, NGC 3079 is outside the observable range of ALMA. The inset shows the angular to linear scale, and the color bar denotes FWHM synthesized beam size. Right Panel: Variability of NGC 3079. The horizontal axis indicates the time difference between observations, while the vertical axis shows the percentage difference in flux density between the two observations.

Table 7. Continuum Flux and Extrapolation to 226 GHz for NGC 3079

Source	Emission	Telescope	Flux[mJy[beam] $^{-1}$]	Frequency[GHz]	beamsize["]	Date[yyyy/mm/dd]
NGC 3079	ν_0	SMA	35.5 ± 2.3	226	5.18	2023/03/16
NGC 3079	Extended-Jet	VLA	$0.487 \pm ^{+2.0}_{-0.4} \pm 0.04$	43	0.047	1998/02/25

NOTE— ν_0 The observation with the smallest beam size between 200–400 GHz. High Dust Extrapolation: Not applicable for this source, as no high frequency observations are available. Low Jet Extrapolation: The lowest extrapolated value of extended-jet is reported. VLBI observations from (Sawada-Satoh et al. 2000), (Irwin & Seaquist 1988; Trotter et al. 1998) are considered as well. We report two uncertainties: the first accounts for source variability (multiplicative factor 5.01) and the second for image noise.

tinction (Schlafly & Finkbeiner 2011). High-frequency ALMA archival data enable minimal variability analyses from 200–400 GHz. As shown in Figure 6, variability is present but modest. The SED of Circinus is shown in Figure 6. It appears that larger-scale structure may exhibit increasing brightness with frequency and lower-scale structure may exhibit decreasing brightness with frequency.

As shown in Table 9, the 259 GHz SMA observation presented in this paper measures a peak flux density of ~ 15 mJy beam $^{-1}$. The thermal-dust contribution is negligible, and the extended-jet contribution from the VLBI extrapolation suggests that no more than half of the total emission arises from extended-jet components. We therefore suggest that at the submm-mm this source primary source of emission is generated from its AGN-core.

22 GHz water masers in this source trace a Keplerian disk at radii ranging from 0.11 ± 0.02 to ~ 0.40 pc from the SMBH, as well as a wide-angle outflow that extends up to ~ 1 pc from the estimated disk center (Greenhill et al. 2003; Hagiwara et al. 2021). In addition to the well-known 22 GHz water maser emission, Circinus has also been observed to exhibit water maser transitions at 183 GHz and 321 GHz (Pesce et al. 2023; Hagiwara et al. 2021). Since 321 GHz water masers have a higher optimal kinetic temperature, they may originate in the accretion disk at radii interior to those traced by the 22 GHz emission. The 321 GHz water maser emission exhibits substantial variability and is coincident with the radio nucleus, indicating a nuclear pumping source. We suggest that submm-mm variability is likewise generated through the same mechanism.

WM components for this source provide interesting insight into the collimation of nuclear outflow in this

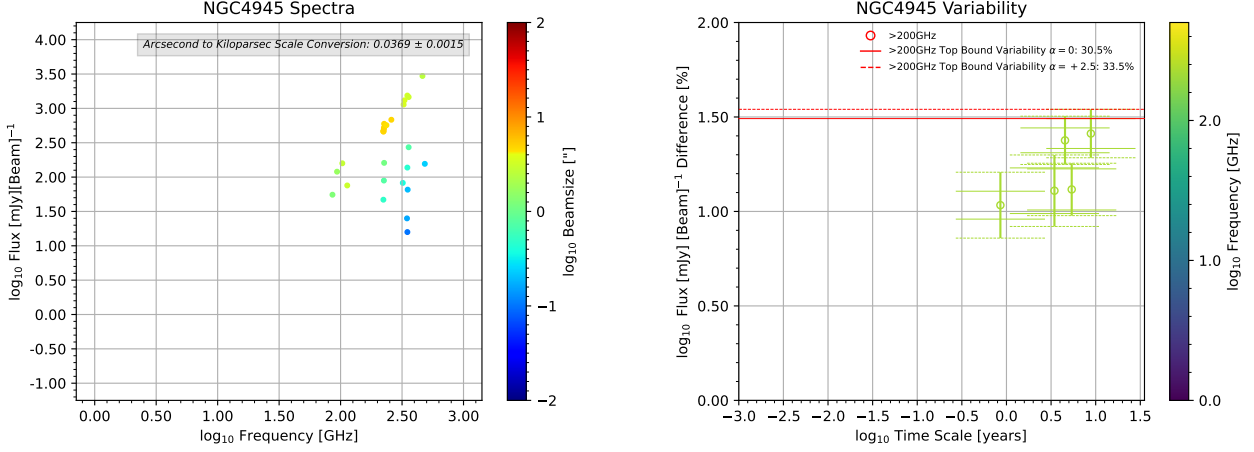


Figure 5. Left Panel: SED of NGC 4945. Data points correspond to continuum observations from ALMA. Due to its southern declination, NGC 4945 is outside the observable range of the SMA and VLA. The inset shows the angular to linear scale, and the color bar denotes FWHM synthesized beam size. Right Panel: Variability of NGC 4945. The horizontal axis indicates the time difference between observations, while the vertical axis shows the percentage difference in flux density between the two observations.

Table 8. Continuum Flux and Extrapolation to 349 GHz for NGC 4945

Source	Emission	Telescope	Flux[mJy[beam] $^{-1}$])	Frequency[GHz]	beamsize["]	Date[yyyy/mm/dd]
NGC 4945	ν_0	ALMA	$15.8^{+6.4}_{-4.5} \pm 0.3$	349	0.078	2023/05/19
NGC 4945	Thermal-Dust	ALMA	0.704 ± 0.041	464	2.69	2023/06/18

NOTE— ν_0 The observation with the smallest beam size between 200–400 GHz. We report two uncertainties: the first accounts for source variability (multiplicative factor 1.40) and the second for image noise. High Dust Extrapolation: The lowest extrapolated value of thermal-dust is reported. Low Jet Extrapolation: Although we obtain an extrapolated value of 27.5 ± 0.4 mJy, we suggest this value is misleading. Emission from this source is dominated by star formation, with free–free emission contributing significantly at cm wavelengths. Thus, we can assume that the jet extrapolation for this source is invalid, since the low-frequency emission is likely dominated by free-free emission that is not present in the submm-mm regime.

obscured source (although 321 GHz components do not seem to trace the outflow), as many components lie outside of the disk and travel at sub-Keplerian velocities (Pesce et al. 2016; Greenhill et al. 2003). The position and motion of these components are attributed to a bipolar, cone-like, wide-angle outflow that extends up to ≈ 1 pc from the estimated disk center, corresponding to material lost from the outer disk; however, the picture is not so clear, as several of these components additionally seem to be affected by radiation emitting from the hot central AGN-core. This model supports a disk-outflow morphology where the warp angle at the inner edge of the disk collimates the nuclear outflow; in other words, the warp angle fixes the orientation of the ionization cone and the illumination patterns observed on larger scales.

4.6. NGC 1068

Among the sources considered, NGC 1068 exhibits the third-largest predicted BHS, with a size of $0.111 \pm 0.005 \mu\text{as}$, as shown in Table 2. 22 GHz water maser measurements constrain the BH mass with a precision of approximately $< 1\%$ and determine the disk inclination angle to be 90° . A SVLBI mission to provide fringe spacing comparable to BHS-scale features would require a baseline approximately 1.6 times longer than the Earth-L2 separation and would need to achieve a brightness sensitivity of ~ 7 mJy at 230 GHz.

The SED of NGC 1068, shown in Figure 7, exhibits a general trend of decreasing brightness with frequency

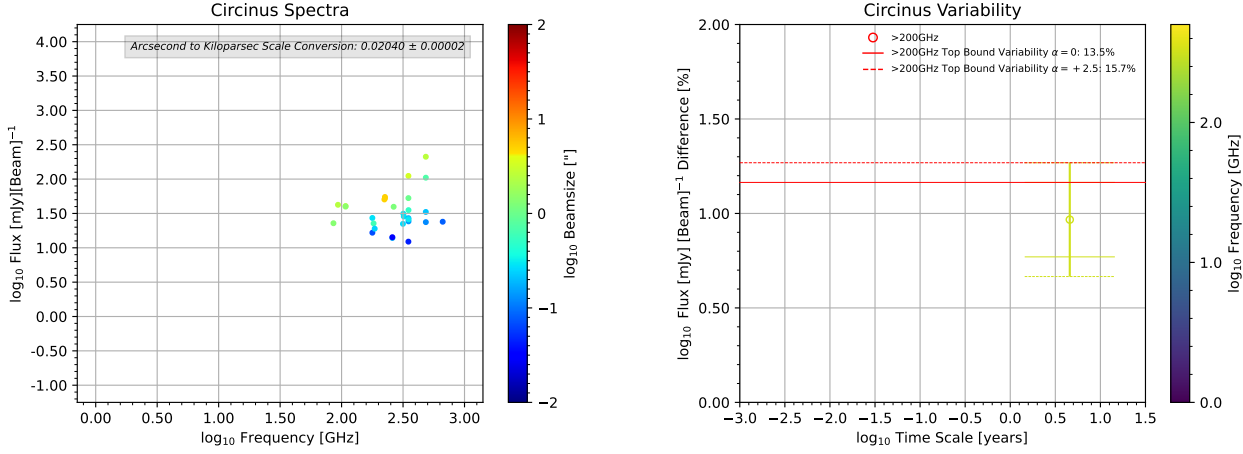


Figure 6. Left Panel: SED of Circinus. Data points correspond to continuum observations from ALMA. Due to its southern declination, Circinus is outside the observable range of the SMA and VLA. The inset shows the angular to linear scale, and the color bar denotes FWHM synthesized beam size. Right Panel: Variability of Circinus. The horizontal axis indicates the time difference between observations, while the vertical axis shows the percentage difference in flux density between the two observations.

Table 9. Continuum Flux and Extrapolation to 259 GHz for Circinus

Source	Emission	Telescope	Flux[mJy[beam] $^{-1}$]	Frequency[GHz]	beamsize["]	Date[yyyy/mm/dd]
Circinus	ν_0	ALMA	$14.27 \pm ^{+2.4} _{-2.1} \pm 0.02$	259	0.026	2019/06/06
Circinus	Thermal-Dust	ALMA	$6.99e-04 \pm 3.1e-05$	484	2.77	2018/10/27
Circinus	Extended-Jet	VLBI ¹	6.70 ± 0.67	2.4	3.25	1994/03-1996/12

NOTE— ν_0 : The observation with the smallest beam size between 200–400 GHz. We report two uncertainties: the first accounts for source variability (multiplicative factor 1.32) and the second for image noise. High Dust Extrapolation: The lowest extrapolated value of thermal-dust is reported. Low Jet Extrapolation: The lowest extrapolated value of extended-jet is reported. VLBI observations from (Elmouttie et al. 1998)¹ are considered as well.

from \sim 1–350 GHz, beyond which it appears to rise – potentially indicating the presence of a “sub-mm bump.” This interpretation is consistent with SED fitting for NGC 1068 in (Mutie et al. 2025). According to this model, the SED also shows a sub-mm excess from 200–700 GHz, consistent with synchrotron emission from an AGN-core; where emission remains optically thick from 200–500 GHz, with the opacity subsequently decreasing toward 700 GHz.

As shown in Table 10, the 351 GHz ALMA observation presented in this paper measures a peak flux density of ~ 7 mJy beam $^{-1}$ and the 351 GHz SMA. The thermal-dust and extended-jet extrapolation contaminations are negligible, suggesting a sub-mm excess, consistent with the findings from Mutie et al. (2025). According to Figure 7, variability of this source is significant in the submm-mm range.

The extrapolated spectral index α in Table 1 indicates a very steeply falling spectrum, in contrast to what we would expect from (Mutie et al. (2025)) and the prediction of an optically thick AGN-core. We refrain from making any physical statements since this value is highly susceptible to dataset-dependent variation not captured by the formal uncertainties, as demonstrated in NGC 4258. However, we note that it does appear to follow the steep SED of NGC 1068 at cm wavelengths.

22 GHz water masers in this source trace a Keplerian disk at radii ranging from 0.35 to 1 pc from the SMBH (Gallimore & Impellizzeri 2023). Searches for water maser emission at 321 GHz and 183 GHz have yielded no detections (Pesce et al. 2016). 22 GHz water maser polarization for this source further indicates that maser filaments trace the magnetic field, constraining

the field orientation and informing the geometry of the circumnuclear disk (Gallimore et al. 2024).

The 22 GHz water masers of this source, and the molecular disk they trace, are rotated by about 30° relative to the elongated plasma-disk component, forming an X-shaped intersection in the sky plane. Assuming a continuous flat-disk morphology, this offset suggests the presence of a strong polar-angle warp at a radius of ~ 0.5 pc from the central engine, where an inner plasma disk transitions into an outer molecular disk (Gallimore et al. 2024). Additionally, water maser filaments are displaced by up to ~ 1 mas (0.07 pc) above the best-fit disk plane (Gallimore et al. 2024), consistent with clouds lifted by hydromagnetic winds into a torus-like structure that obscures the central engine at certain viewing angles, as required in unified AGN schemes. The location of the water masers, therefore, potentially marks the base of the outflow region.

Beyond the water masers orbiting the SMBH in this source, there are two additional sets of 22 GHz water maser components. The first additional set exhibits a ring-like distribution that suggests either a jet collision with a molecular cloud (Morishima et al. 2022; Gallimore & Impellizzeri 2023). The second additional set of water masers traces a wide-angle outflow, similar to that observed in the Circinus Galaxy.

5. FUTURE WORK

The flux estimates for CGCG 074-064 and J0437+2456 could not be located in the 200-400 GHz range from the ALMA or VLA archives, nor were these sources included in the SMA observations presented in this paper. Future work should incorporate continuum imaging in the submm-mm regime for these sources. Additionally, extrapolation of α has been shown to be inconsistent due to statistical uncertainty; to obtain a more reliable estimate of α , we recommend acquiring and imaging additional SMA observations for NGC 4258, NGC 3079, and NGC 1068.

To better constrain variability and refine estimates of emission brightness and turnover frequencies, multi-epoch, high-resolution continuum observations in the submm-mm range would be useful. With better sampled data, we would also be able to analyze compactness—an aspect neglected in this paper—in a manner similar to the approach used in Sec 3.5. Instead of searching for pairs of observations that match in frequency and beam size to measure flux differences, we could search for pairs that match in flux and frequency, and then examine the differences in beam size. With VLBI, variability can be

entirely decoupled from compactness by analyzing different baselines of data taken at the same epoch.

Although 22 GHz water masers will remain the most commonly observed transition due to their relatively broad range of excitation densities and temperatures, water masers at transitions beyond 22 GHz provide a valuable diagnostic of the physical conditions and excitation mechanisms within AGN accretion disks, and continued searches for such lines remain essential. As discussed in Section 3.3, such higher-frequency water masers would provide the opportunity to probe SMBH spin through the BHS-water maser dynamical-center offset without the need for cross-band calibration between 22 GHz and 230 GHz.

6. CONCLUSION

Among known water maser systems, NGC 4258 is the leading target: its predicted BHS is 0.617 ± 0.049 μ as, and a baseline from Earth to L2 delivers $\theta \approx 0.18$ μ as – comfortably resolving the BHS. With a ~ 10 mJy AGN-core at 230 GHz, a space-ground baseline meeting typical SEFD/bandwidth assumptions attains the required fringe SNR for detection. Our results for this source further suggest that the disk in NGC 4258 remains thin down to a transitional radius of $\lesssim 100 R_S$, within which it transitions into an ADAF (Lasota et al. 1996; Herrnstein (1998a); Herrnstein et al. (2005)).

A central contribution of this work is a spin observable: the BHS-megamaser disk dynamical-center offset. The maximal offset is $\sigma_\theta \simeq 0.14\theta_{\text{BHS}}$; for NGC 4258, this implies $\sigma_\theta \approx 0.09$ μ as. At 230 GHz, an Earth-Moon baseline provides the necessary astrometric precision with a SNR of 3.6 ± 0.3 . The remaining gate is simultaneous 22 GHz water maser astrometry: current astrometric uncertainty of the water maser dynamical center is ~ 5 μ as, and achieving $\lesssim 0.09$ μ as requires a ~ 55 precision gain.

Beyond NGC 4258, all megamaser disk AGN require baselines extending beyond Earth-L2. Baselines reaching Earth-L4/L5 recover nearly all BHS-scale fringe spacings for the water maser sample. A handful of the brightest sources in the submm-mm have flux densities of $\gtrsim 10$ mJy and resolving these sources may become feasible in the distant future.

The relatively high flux of NGC 3079 makes this source accessible to instruments with modest sensitivity, and its disk geometry may be similar to that inferred for NGC 1068 from water-maser measurements (Kondratico et al. 2005; Gallimore et al. 2024). Although notably faint, NGC 1194 emerges as a particularly compelling target due to its distance, which may enable the inclusion of higher-order gravitational redshift correc-

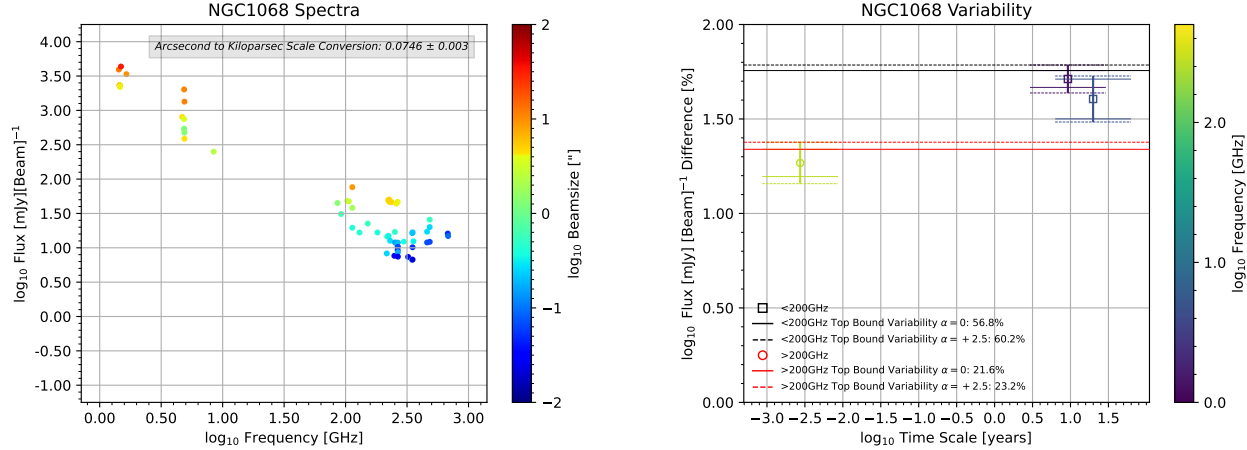


Figure 7. Left Panel: SED of NGC 1068. Data points correspond to continuum observations from the SMA, ALMA, and VLA. The inset shows the angular to linear scale, and the color bar denotes FWHM synthesized beam size. Right Panel: Variability of NGC 1068. The horizontal axis indicates the time difference between observations, while the vertical axis shows the percentage difference in flux density between the two observations.

Table 10. Continuum Flux and Extrapolation to 351 GHz for NGC 1068

Source	Emission	Telescope	Flux[mJy[beam] $^{-1}$]	Frequency[GHz]	beamsize["]	Date[yyyy/mm/dd]
NGC 1068	ν_0	ALMA	$6.74^{+3.0}_{-2.1} \pm 0.04$	351	0.014	2021/09/03
NGC 1068	Thermal-Dust	ALMA	0.00475 ± 0.00021	483	0.56	2018/05/24
NGC 1068	Extended-Jet	VLBI ¹	$0.11307^{+0.1}_{-0.05} \pm 3e-05$	22	0.00083	2021/11/14

NOTE— ν_0 : The observation with the smallest beam size between 200–400 GHz. We report two uncertainties: the first accounts for source variability (multiplicative factor 1.44) and the second for image noise. High Dust Extrapolation: The lowest extrapolated value of thermal-dust is reported. Low Jet Extrapolation: The lowest extrapolated value of extended-jet is reported. VLBI observations from (Gallimore et al. 2024)¹, (Greenhill et al. 1996; Ulvestad et al. 1987; Krips, M. et al. 2006) are considered as well. We report two uncertainties: the first accounts for source variability (multiplicative factor 1.79) and the second for image noise.

tions in water maser-based dynamical modeling (Vilalaraos et al. 2022). NGC 4945 is a valuable laboratory for studying the interplay between edge-on AGN and starburst activity in highly obscured galactic environments (Marconi et al. 2000; Spoon et al. 2003; Pérez-Beaupuits et al. 2011; Emig et al. 2020). Water masers in Circinus remain valuable for studying the interplay between nuclear outflow, inflow, and disk morphology (Pesce et al. 2016; Greenhill et al. 2003; Hagiwara et al. 2021). Last but not least, NGC 1068: when interpreted alongside prospective BHS imaging, the filamentary alignment, polarization structure, vertical displacement, and plasma-molecular offsets traced by the water masers in NGC 1068 provide a uniquely complementary probe of parsec-scale magnetic geometry, offering constraints on disk-outflow coupling and enabling tests

of whether large-scale asymmetries arise from magnetic regulation of the inner accretion flow rather than purely from spin- or inclination-driven effects (Morishima et al. 2022; Gallimore & Impellizzeri 2023; Gallimore et al. 2024).

This work was supported by the National Science Foundation (NSF) under grant AST-2034306. This research made use of the NASA/IPAC Extragalactic Database (NED) and of observations obtained with the Submillimeter Array (SMA) under programs 2022B-H002 and 2021B-H004, as well as Atacama Large Millimeter/submillimeter Array (ALMA) and Karl G. Jansky Very Large Array (VLA) data retrieved from their respective science archives. We acknowledge that the SMA is located on Maunakea, a site of profound cultural and spiritual significance to the Kānaka Maoli; that ALMA is located on the ancestral lands of the Likan Antai (Atacameño) People; and that the VLA is located on land of long-standing cultural significance to Indigenous peoples of the Socorro region. We are grateful for the privilege of studying the cosmos from these lands. The SMA is a joint project between the Smithsonian Astrophysical Observatory and the Academia Sinica Institute of Astronomy and Astrophysics and is funded by the Smithsonian Institution and the Academia Sinica. The National Radio Astronomy Observatory (NRAO) and Green Bank Observatory are facilities of the U.S. National Science Foundation operated under cooperative agreement by Associated Universities, Inc. ALMA is a partnership of ESO (representing its member states), NSF (USA), and NINS (Japan), together with NRC (Canada), NSTC and ASIAA (Taiwan), and KASI (Republic of Korea), in cooperation with the Republic of Chile. The Joint ALMA Observatory is operated by ESO, AUI/NRAO, and NAOJ.

Facilities: SMA, ALMA, VLA

Software: WM-AGN Analysis Code ([Burridge 2026](#))

REFERENCES

- Akiyama, K., Niinuma, K., Hada, K., et al. 2024, in Space Telescopes and Instrumentation 2024: Optical, Infrared, and Millimeter Wave, ed. L. E. Coyle, M. D. Perrin, & S. Matsuura (SPIE), 91, doi: [10.1117/12.3019968](https://doi.org/10.1117/12.3019968)
- Albareti, F. D., Allende Prieto, C., Almeida, A., et al. 2017, *ApJS*, 233, 25, doi: [10.3847/1538-4365/aa8992](https://doi.org/10.3847/1538-4365/aa8992)
- Andrianov, A. S., Baryshev, A. M., Falcke, H., et al. 2020, *Monthly Notices of the Royal Astronomical Society*, 500, 4866, doi: [10.1093/mnras/staa2709](https://doi.org/10.1093/mnras/staa2709)
- Baer-Way, R., DeGraw, A., Zheng, W., et al. 2024, *ApJ*, 964, 172, doi: [10.3847/1538-4357/ad2175](https://doi.org/10.3847/1538-4357/ad2175)
- Bardeen. 1973, Black Holes (New York: Gordon and Breach)
- Bendo, G. J., Henkel, C., D'Cruze, M. J., et al. 2016, *Monthly Notices of the Royal Astronomical Society*, 463, 252, doi: [10.1093/mnras/stw1659](https://doi.org/10.1093/mnras/stw1659)
- Blandford, R. D., & Königl, A. 1979, *ApJ*, 232, 34, doi: [10.1086/157262](https://doi.org/10.1086/157262)
- Blandford, R. D., & Ostriker, J. P. 1978, *ApJL*, 221, L29, doi: [10.1086/182658](https://doi.org/10.1086/182658)
- Bolatto, A. D., Wolfire, M., & Leroy, A. K. 2013, *ARA&A*, 51, 207, doi: [10.1146/annurev-astro-082812-140944](https://doi.org/10.1146/annurev-astro-082812-140944)
- Bower, G. C., Dexter, J., Markoff, S., et al. 2015, *ApJL*, 811, L6, doi: [10.1088/2041-8205/811/1/L6](https://doi.org/10.1088/2041-8205/811/1/L6)
- Brightman, M., & Nandra, K. 2011, *Monthly Notices of the Royal Astronomical Society*, 413, 1206, doi: [10.1111/j.1365-2966.2011.18207.x](https://doi.org/10.1111/j.1365-2966.2011.18207.x)
- Bronzwaer, T., Davelaar, J., Younsi, Z., et al. 2020, *Monthly Notices of the Royal Astronomical Society*, 501, 4722, doi: [10.1093/mnras/staa3430](https://doi.org/10.1093/mnras/staa3430)
- Burridge, R. 2026, RomanBurridge/Burridge2025-WM-AGN-Analysis, Zenodo, doi: [10.5281/zenodo.1813578](https://doi.org/10.5281/zenodo.1813578)

- Burt, E., Ely, T., Bower, G., et al. 2025, Frequency Standard Contributions to Limitations on the Signal-to-Noise Ratio in Very Long Baseline Interferometric (VLBI) Observations. <https://arxiv.org/abs/2508.19123>
- Cackett, E. M., Bentz, M. C., & Kara, E. 2021, *iScience*, 24, 102557, doi: [10.11016/j.isci.2021.102557](https://doi.org/10.11016/j.isci.2021.102557)
- Casey, C. M. 2012, *MNRAS*, 425, 3094, doi: [10.1111/j.1365-2966.2012.21455.x](https://doi.org/10.1111/j.1365-2966.2012.21455.x)
- Chen, B.-Y., Bower, G. C., Dexter, J., et al. 2023, *The Astrophysical Journal*, 951, 93, doi: [10.3847/1538-4357/acd250](https://doi.org/10.3847/1538-4357/acd250)
- Do, T., Hees, A., Ghez, A., et al. 2019, *Science*, 365, 664, doi: [10.1126/science.aav8137](https://doi.org/10.1126/science.aav8137)
- Doi, A., Kamenó, S., Kohno, K., Nakanishi, K., & Inoue, M. 2005, *Monthly Notices of the Royal Astronomical Society*, 363, 692, doi: [10.1111/j.1365-2966.2005.09471.x](https://doi.org/10.1111/j.1365-2966.2005.09471.x)
- Efstathiou, A., Farrah, D., Afonso, J., et al. 2021, *Monthly Notices of the Royal Astronomical Society*, 512, 5183–5213, doi: [10.1093/mnras/stab3642](https://doi.org/10.1093/mnras/stab3642)
- Elmouttie, M., Haynes, R. F., Jones, K. L., Sadler, E. M., & Ehle, M. 1998, *Monthly Notices of the Royal Astronomical Society*, 297, 1202, doi: [10.1046/j.1365-8711.1998.01592.x](https://doi.org/10.1046/j.1365-8711.1998.01592.x)
- Emig, K. L., Bolatto, A. D., Leroy, A. K., et al. 2020, *The Astrophysical Journal*, 903, 50, doi: [10.3847/1538-4357/abb67d](https://doi.org/10.3847/1538-4357/abb67d)
- Event Horizon Telescope Collaboration, Akiyama, K., Alberdi, A., et al. 2019b, *The Astrophysical Journal Letters*, 875, L2, doi: [10.3847/2041-8213/ab0c96](https://doi.org/10.3847/2041-8213/ab0c96)
- . 2019f, *The Astrophysical Journal Letters*, 875, L6, doi: [10.3847/2041-8213/ab1141](https://doi.org/10.3847/2041-8213/ab1141)
- . 2021b, *ApJL*, 910, L13, doi: [10.3847/2041-8213/abe4de](https://doi.org/10.3847/2041-8213/abe4de)
- . 2022d, *The Astrophysical Journal Letters*, 930, L15, doi: [10.3847/2041-8213/ac6736](https://doi.org/10.3847/2041-8213/ac6736)
- . 2022e, *The Astrophysical Journal Letters*, 930, L16, doi: [10.3847/2041-8213/ac6672](https://doi.org/10.3847/2041-8213/ac6672)
- . 2022f, *The Astrophysical Journal Letters*, 930, L17, doi: [10.3847/2041-8213/ac6756](https://doi.org/10.3847/2041-8213/ac6756)
- Fabian, A. C. 2012, *ARA&A*, 50, 455, doi: [10.1146/annurev-astro-081811-125521](https://doi.org/10.1146/annurev-astro-081811-125521)
- Fabian, A. C., Barcons, X., Almaini, O., & Iwasawa, K. 1998, *Monthly Notices of the Royal Astronomical Society*, 297, L11, doi: [10.1046/j.1365-8711.1998.01645.x](https://doi.org/10.1046/j.1365-8711.1998.01645.x)
- Fischer, T. C., Johnson, M. C., Secrest, N. J., Crenshaw, D. M., & Kraemer, S. B. 2023, *The Astrophysical Journal*, 953, 87, doi: [10.3847/1538-4357/ace1f0](https://doi.org/10.3847/1538-4357/ace1f0)
- Gallimore, J. F., Baum, S. A., & O'Dea, C. P. 2004, *ApJ*, 613, 794, doi: [10.1086/423167](https://doi.org/10.1086/423167)
- Gallimore, J. F., & Impellizzeri, C. M. V. 2023, *The Astrophysical Journal*, 951, 109, doi: [10.3847/1538-4357/acd846](https://doi.org/10.3847/1538-4357/acd846)
- Gallimore, J. F., Impellizzeri, C. M. V., Aghelpasand, S., et al. 2024, *The Discovery of Polarized Water Vapor Megamaser Emission in a Molecular Accretion Disk*. <https://arxiv.org/abs/2410.10569>
- Gao, F., Braatz, J. A., Reid, M. J., et al. 2016b, *The Astrophysical Journal*, 834, 52, doi: [10.3847/1538-4357/834/1/52](https://doi.org/10.3847/1538-4357/834/1/52)
- Gebhardt, K., Adams, J., Richstone, D., et al. 2011, *The Astrophysical Journal*, 729, 119, doi: [10.1088/0004-637X/729/2/119](https://doi.org/10.1088/0004-637X/729/2/119)
- Gezari, S. 2021, *ARA&A*, 59, 21, doi: [10.1146/annurev-astro-111720-030029](https://doi.org/10.1146/annurev-astro-111720-030029)
- Gliozzi, M., Williams, J. K., & Michel, D. A. 2021, *Monthly Notices of the Royal Astronomical Society*, 502, 3329–3342, doi: [10.1093/mnras/stab181](https://doi.org/10.1093/mnras/stab181)
- Goulding, A. D., & Alexander, D. M. 2009, *Monthly Notices of the Royal Astronomical Society*, 398, 1165, doi: [10.1111/j.1365-2966.2009.15194.x](https://doi.org/10.1111/j.1365-2966.2009.15194.x)
- GRAVITY Collaboration, Abuter, R., Aimar, N., et al. 2022, *A&A*, 657, L12, doi: [10.1051/0004-6361/202142465](https://doi.org/10.1051/0004-6361/202142465)
- Gray, M. D., Baudry, A., Richards, A. M. S., et al. 2015, *Monthly Notices of the Royal Astronomical Society*, 456, 374, doi: [10.1093/mnras/stv2437](https://doi.org/10.1093/mnras/stv2437)
- Greene, J. E., Seth, A., Kim, M., et al. 2016, *The Astrophysical Journal Letters*, 826, L32, doi: [10.3847/2041-8205/826/2/L32](https://doi.org/10.3847/2041-8205/826/2/L32)
- Greenhill, L. J., Gwinn, C. R., Antonucci, R., & Barvainis, R. 1996, *The Astrophysical Journal*, 472, L21, doi: [10.1086/310346](https://doi.org/10.1086/310346)
- Greenhill, L. J., Moran, J. M., & Herrnstein, J. R. 1997, *ApJL*, 481, L23, doi: [10.1086/310643](https://doi.org/10.1086/310643)
- Greenhill, L. J., Booth, R. S., Ellingsen, S. P., et al. 2003, *ApJ*, 590, 162, doi: [10.1086/374862](https://doi.org/10.1086/374862)
- Hagiwara, Y., Horiuchi, S., Imanishi, M., & Edwards, P. G. 2021, *The Astrophysical Journal*, 923, 251, doi: [10.3847/1538-4357/ac3089](https://doi.org/10.3847/1538-4357/ac3089)
- Heckman, T. M., & Best, P. N. 2014, *ARA&A*, 52, 589, doi: [10.1146/annurev-astro-081913-035722](https://doi.org/10.1146/annurev-astro-081913-035722)
- Herrnstein, J. R. 1998a, in *IAU Symposium*, Vol. 184, *The Central Regions of the Galaxy and Galaxies*, ed. Y. Sofue, 395
- Herrnstein, J. R., Greenhill, L. J., Moran, J. M., et al. 1998b, *The Astrophysical Journal*, 497, L69, doi: [10.1086/311284](https://doi.org/10.1086/311284)
- Herrnstein, J. R., Moran, J. M., Greenhill, L. J., & Trotter, A. S. 2005, *ApJ*, 629, 719, doi: [10.1086/431421](https://doi.org/10.1086/431421)

- Hong, X., Wu, W., Liu, Q., et al. 2025, Lunar Orbital VLBI Experiment: motivation, scientific purposes and status. <https://arxiv.org/abs/2507.16317>
- Hovatta, T., Tornikoski, M., Lainela, M., et al. 2007, *Astronomy & Astrophysics*, 469, 899–912, doi: [10.1051/0004-6361:20077529](https://doi.org/10.1051/0004-6361:20077529)
- Huchra, J. P., Vogeley, M. S., & Geller, M. J. 1999, *ApJS*, 121, 287, doi: [10.1086/313194](https://doi.org/10.1086/313194)
- Humphreys, E. M. L., Greenhill, L. J., Reid, M. J., et al. 2005, *ApJL*, 634, L133, doi: [10.1086/498890](https://doi.org/10.1086/498890)
- Humphreys, E. M. L., Reid, M. J., Greenhill, L. J., Moran, J. M., & Argon, A. L. 2008, *ApJ*, 672, 800, doi: [10.1086/523637](https://doi.org/10.1086/523637)
- Humphreys, E. M. L., Vlemmings, W. H. T., Impellizzeri, C. M. V., et al. 2016, *Astronomy & Astrophysics*, 592, L13, doi: [10.1051/0004-6361/201629168](https://doi.org/10.1051/0004-6361/201629168)
- Inoue, Y., & Doi, A. 2014, *Publications of the Astronomical Society of Japan*, 66, L8, doi: [10.1093/pasj/psu079](https://doi.org/10.1093/pasj/psu079)
- Irwin, J. A., & Seaquist, E. R. 1988, *ApJ*, 335, 658, doi: [10.1086/166956](https://doi.org/10.1086/166956)
- Issaoun, S., Alonso, K., Akiyama, K., et al. 2024, in *Space Telescopes and Instrumentation 2024: Optical, Infrared, and Millimeter Wave*, ed. L. E. Coyle, M. D. Perrin, & S. Matsuura (SPIE), 193, doi: [10.1117/12.3020041](https://doi.org/10.1117/12.3020041)
- Jiang, W., Zhao, G.-Y., Shen, Z.-Q., et al. 2022, Applications of the source-frequency phase-referencing technique for ngEHT observations. <https://arxiv.org/abs/2212.08994>
- Johnson, M., Akiyama, K., Baturin, R., et al. 2024, in *Space Telescopes and Instrumentation 2024: Optical, Infrared, and Millimeter Wave*, ed. L. E. Coyle, M. D. Perrin, & S. Matsuura (SPIE), 90, doi: [10.1117/12.3019835](https://doi.org/10.1117/12.3019835)
- Kamali, F., Henkel, C., Brunthaler, A., et al. 2017, *A&A*, 605, A84, doi: [10.1051/0004-6361/201730899](https://doi.org/10.1051/0004-6361/201730899)
- Kanehisa, K. J., Pawlowski, M. S., Müller, O., & Sohn, S. T. 2023, *MNRAS*, 519, 6184, doi: [10.1093/mnras/stad061](https://doi.org/10.1093/mnras/stad061)
- Kellermann, K. I., & Pauliny-Toth, I. I. K. 1981, *ARA&A*, 19, 373, doi: [10.1146/annurev.aa.19.090181.002105](https://doi.org/10.1146/annurev.aa.19.090181.002105)
- Kennicutt, R. C., & Evans, N. J. 2012, *ARA&A*, 50, 531, doi: [10.1146/annurev-astro-081811-125610](https://doi.org/10.1146/annurev-astro-081811-125610)
- Kondratko, P. T., Greenhill, L. J., & Moran, J. M. 2005, *ApJ*, 618, 618, doi: [10.1086/426101](https://doi.org/10.1086/426101)
- Kormendy, J., & Ho, L. C. 2013, *ARA&A*, 51, 511, doi: [10.1146/annurev-astro-082708-101811](https://doi.org/10.1146/annurev-astro-082708-101811)
- Koss, M. J., Trakhtenbrot, B., Ricci, C., et al. 2022, *ApJS*, 261, 6, doi: [10.3847/1538-4365/ac650b](https://doi.org/10.3847/1538-4365/ac650b)
- Krips, M., Eckart, A., Neri, R., et al. 2006, *A&A*, 446, 113, doi: [10.1051/0004-6361:20053729](https://doi.org/10.1051/0004-6361:20053729)
- Kuo, C. Y., Braatz, J. A., Condon, J. J., et al. 2010, *The Astrophysical Journal*, 727, 20, doi: [10.1088/0004-637X/727/1/20](https://doi.org/10.1088/0004-637X/727/1/20)
- Lasota, J. P., Abramowicz, M. A., Chen, X., et al. 1996, *ApJ*, 462, 142, doi: [10.1086/177137](https://doi.org/10.1086/177137)
- Lenc, E., & Tingay, S. J. 2009, *AJ*, 137, 537, doi: [10.1088/0004-6256/137/1/537](https://doi.org/10.1088/0004-6256/137/1/537)
- Liepold, E. R., Ma, C.-P., & Walsh, J. L. 2023, *The Astrophysical Journal Letters*, 945, L35, doi: [10.3847/2041-8213/acbbcf](https://doi.org/10.3847/2041-8213/acbbcf)
- Likhachev, S. F., Rudnitskiy, A. G., Shchurov, M. A., et al. 2022, *Monthly Notices of the Royal Astronomical Society*, 511, 668–682, doi: [10.1093/mnras/stac079](https://doi.org/10.1093/mnras/stac079)
- Lister, M. L., Cohen, M. H., Homan, D. C., et al. 2009, *AJ*, 138, 1874, doi: [10.1088/0004-6256/138/6/1874](https://doi.org/10.1088/0004-6256/138/6/1874)
- Lo, K. Y. 2005, *ARA&A*, 43, 625, doi: [10.1146/annurev.astro.41.011802.094927](https://doi.org/10.1146/annurev.astro.41.011802.094927)
- Lu, N. Y., Hoffman, G. L., Groff, T., Roos, T., & Lamphier, C. 1993, *ApJS*, 88, 383, doi: [10.1086/191826](https://doi.org/10.1086/191826)
- Mahadevan, R. 1997, *ApJ*, 477, 585, doi: [10.1086/303727](https://doi.org/10.1086/303727)
- Marconi, A., Oliva, E., van der Werf, P. P., et al. 2000, *A&A*, 357, 24, doi: [10.48550/arXiv.astro-ph/0002244](https://doi.org/10.48550/arXiv.astro-ph/0002244)
- Martín, S., Mangum, J. G., Harada, N., et al. 2021, *Astronomy & Astrophysics*, 656, A46, doi: [10.1051/0004-6361/202141567](https://doi.org/10.1051/0004-6361/202141567)
- Menten, K. M., & Young, K. 1995, *ApJL*, 450, L67, doi: [10.1086/316776](https://doi.org/10.1086/316776)
- Middelberg, E., Krichbaum, T. P., Roy, A. L., Witzel, A., & Zensus, J. A. 2003, Approaching NGC3079 with VLBI. <https://arxiv.org/abs/astro-ph/0309382>
- Moorwood, A. F. M., van der Werf, P. P., Kotilainen, J. K., Marconi, A., & Oliva, E. 1996, *A&A*, 308, L1
- Morishima, Y., Sudou, H., Yamauchi, A., Taniguchi, Y., & Nakai, N. 2022, *Publications of the Astronomical Society of Japan*, 75, 71, doi: [10.1093/pasj/psac092](https://doi.org/10.1093/pasj/psac092)
- Murphy, E. J., Condon, J. J., Schinnerer, E., et al. 2011, *ApJ*, 737, 67, doi: [10.1088/0004-637X/737/2/67](https://doi.org/10.1088/0004-637X/737/2/67)
- Mutie, I. M., del Palacio, S., Beswick, R. J., et al. 2025, *Monthly Notices of the Royal Astronomical Society*, 539, 808, doi: [10.1093/mnras/staf524](https://doi.org/10.1093/mnras/staf524)
- Mutie, I. M., Williams-Baldwin, D., Beswick, R. J., et al. 2024, *Monthly Notices of the Royal Astronomical Society*, 527, 11756, doi: [10.1093/mnras/stad3864](https://doi.org/10.1093/mnras/stad3864)
- Muxlow, T. W. B., Pedlar, A., Holloway, A. J., Gallimore, J. F., & Antonucci, R. R. J. 1996, *MNRAS*, 278, 854, doi: [10.1093/mnras/278.3.854](https://doi.org/10.1093/mnras/278.3.854)
- Narayan, R., & Yi, I. 1995, *ApJ*, 444, 231, doi: [10.1086/175599](https://doi.org/10.1086/175599)

- Nesterenok, A. V. 2015, Monthly Notices of the Royal Astronomical Society, 449, 2875, doi: [10.1093/mnras/stv485](https://doi.org/10.1093/mnras/stv485)
- Novikov, I. D., Likhachev, S. F., Shchekinov, Y. A., et al. 2021, Physics Uspekhi, 64, 386, doi: [10.3367/UFNe.2020.12.038898](https://doi.org/10.3367/UFNe.2020.12.038898)
- Pérez-Beaupuits, J. P., Spoon, H. W. W., Spaans, M., & Smith, J. D. 2011, A&A, 533, A56, doi: [10.1051/0004-6361/201117153](https://doi.org/10.1051/0004-6361/201117153)
- Pesce, D., Haworth, K., Melnick, G. J., et al. 2019, in Bulletin of the American Astronomical Society, Vol. 51, 176, doi: [10.48550/arXiv.1909.01408](https://doi.org/10.48550/arXiv.1909.01408)
- Pesce, D. W., Braatz, J. A., Condon, J. J., et al. 2015, The Astrophysical Journal, 810, 65, doi: [10.1088/0004-637X/810/1/65](https://doi.org/10.1088/0004-637X/810/1/65)
- Pesce, D. W., Braatz, J. A., Condon, J. J., & Greene, J. E. 2018, ApJ, 863, 149, doi: [10.3847/1538-4357/aad3c2](https://doi.org/10.3847/1538-4357/aad3c2)
- Pesce, D. W., Braatz, J. A., Henkel, C., et al. 2023, The Astrophysical Journal, 948, 134, doi: [10.3847/1538-4357/acc57a](https://doi.org/10.3847/1538-4357/acc57a)
- Pesce, D. W., Braatz, J. A., & Impellizzeri, C. M. V. 2016, The Astrophysical Journal, 827, 68, doi: [10.3847/0004-637X/827/1/68](https://doi.org/10.3847/0004-637X/827/1/68)
- Pesce, D. W., Braatz, J. A., Reid, M. J., et al. 2020a, ApJ, 890, 118, doi: [10.3847/1538-4357/ab6bcd](https://doi.org/10.3847/1538-4357/ab6bcd)
- . 2020b, The Astrophysical Journal Letters, 891, L1, doi: [10.3847/2041-8213/ab75f0](https://doi.org/10.3847/2041-8213/ab75f0)
- Pesce, D. W., Palumbo, D. C. M., Narayan, R., et al. 2021, The Astrophysical Journal, 923, 260, doi: [10.3847/1538-4357/ac2eb5](https://doi.org/10.3847/1538-4357/ac2eb5)
- Prieto, M. A., Meisenheimer, K., Marco, O., et al. 2004, The Astrophysical Journal, 614, 135, doi: [10.1086/423422](https://doi.org/10.1086/423422)
- Reid, M. J., Pesce, D. W., & Riess, A. G. 2019, ApJL, 886, L27, doi: [10.3847/2041-8213/ab552d](https://doi.org/10.3847/2041-8213/ab552d)
- Reid, M. J., Schneps, M. H., Moran, J. M., et al. 1988, ApJ, 330, 809, doi: [10.1086/166514](https://doi.org/10.1086/166514)
- Ressler, S. M., White, C. J., & Quataert, E. 2023, Monthly Notices of the Royal Astronomical Society, 521, 4277, doi: [10.1093/mnras/stad837](https://doi.org/10.1093/mnras/stad837)
- Riffel, R., Rodríguez-Ardila, A., Aleman, I., et al. 2013, MNRAS, 430, 2002, doi: [10.1093/mnras/stt026](https://doi.org/10.1093/mnras/stt026)
- Rybicki, G. B., & Lightman, A. P. 1979, Radiative processes in astrophysics
- Salehi, K., Walia, R. K., Chang, D., & Kocherlakota, P. 2024, Influence of Observer Inclination and Spacetime Structure on Photon Ring Observables. <https://arxiv.org/abs/2411.15310>
- Sawada-Satoh, S., Inoue, M., Shibata, K. M., et al. 2000, PASJ, 52, 421, doi: [10.1093/pasj/52.3.421](https://doi.org/10.1093/pasj/52.3.421)
- Schlafly, E. F., & Finkbeiner, D. P. 2011, ApJ, 737, 103, doi: [10.1088/0004-637X/737/2/103](https://doi.org/10.1088/0004-637X/737/2/103)
- Shabala, S. S., Santoso, J. S., & Godfrey, L. E. H. 2012, The Astrophysical Journal, 756, 161, doi: [10.1088/0004-637x/756/2/161](https://doi.org/10.1088/0004-637x/756/2/161)
- Simon, D. A., Cappellari, M., & Hartke, J. 2024, MNRAS, 527, 2341, doi: [10.1093/mnras/stad3309](https://doi.org/10.1093/mnras/stad3309)
- Spoon, H. W. W., Moorwood, A. F. M., Pontoppidan, K. M., et al. 2003, A&A, 402, 499, doi: [10.1051/0004-6361:20030290](https://doi.org/10.1051/0004-6361:20030290)
- Springob, C. M., Haynes, M. P., Giovanelli, R., & Kent, B. R. 2005, ApJS, 160, 149, doi: [10.1086/431550](https://doi.org/10.1086/431550)
- Syachina, T. A., Rudnitskiy, A. G., Mzhelskiy, P. V., Shchurov, M. A., & Zapevalin, P. R. 2024, Orbit Design for the Millimetron Space Observatory. <https://arxiv.org/abs/2410.20847>
- Takahashi, R. 2004, ApJ, 611, 996, doi: [10.1086/422403](https://doi.org/10.1086/422403)
- Thater, S., Krajnović, D., Weilbacher, P. M., et al. 2021, Monthly Notices of the Royal Astronomical Society, 509, 5416, doi: [10.1093/mnras/stab3210](https://doi.org/10.1093/mnras/stab3210)
- Theureau, G., Coudreau, N., Hallet, N., Hanski, M. O., & Poulain, M. 2017, A&A, 599, A104, doi: [10.1051/0004-6361/201629813](https://doi.org/10.1051/0004-6361/201629813)
- Trotter, A. S., Greenhill, L. J., Moran, J. M., et al. 1998, ApJ, 495, 740, doi: [10.1086/305335](https://doi.org/10.1086/305335)
- Trześniewski, T., Czerny, B., Karas, V., et al. 2011, A&A, 530, A136, doi: [10.1051/0004-6361/201016369](https://doi.org/10.1051/0004-6361/201016369)
- Tully, R. B., Rizzi, L., Shaya, E. J., et al. 2009, The Astronomical Journal, 138, 323, doi: [10.1088/0004-6256/138/2/323](https://doi.org/10.1088/0004-6256/138/2/323)
- Ulvestad, J. S., Neff, S. G., & Wilson, A. S. 1987, AJ, 93, 22, doi: [10.1086/114286](https://doi.org/10.1086/114286)
- Villaraos, D., Herrera-Aguilar, A., Nucamendi, U., González-Juárez, G., & Lizardo-Castro, R. 2022, Monthly Notices of the Royal Astronomical Society, 517, 4213, doi: [10.1093/mnras/stac2973](https://doi.org/10.1093/mnras/stac2973)
- Walker, R. C. 1995, in Astronomical Society of the Pacific Conference Series, Vol. 82, Very Long Baseline Interferometry and the VLBA, ed. J. A. Zensus, P. J. Diamond, & P. J. Napier, 133
- Walsh, J. L., Barth, A. J., Ho, L. C., & Sarzi, M. 2013, The Astrophysical Journal, 770, 86, doi: [10.1088/0004-637X/770/2/86](https://doi.org/10.1088/0004-637X/770/2/86)
- Wielgus, M., Marchili, N., Martí-Vidal, I., et al. 2022, ApJL, 930, L19, doi: [10.3847/2041-8213/ac6428](https://doi.org/10.3847/2041-8213/ac6428)
- Yang, Y., Li, B., Wilson, A. S., & Reynolds, C. S. 2007, ApJ, 660, 1106, doi: [10.1086/512966](https://doi.org/10.1086/512966)
- Zhang, H., Bureau, M., Smith, M. D., et al. 2024, Monthly Notices of the Royal Astronomical Society, 530, 3240, doi: [10.1093/mnras/stae1106](https://doi.org/10.1093/mnras/stae1106)

- Zhang, X. A., Ricarte, A., Pesce, D. W., et al. 2025, The Astrophysical Journal, 985, 41,
doi: [10.3847/1538-4357/adbd45](https://doi.org/10.3847/1538-4357/adbd45)
- Zhao, W., Braatz, J. A., Condon, J. J., et al. 2018, ApJ, 854, 124, doi: [10.3847/1538-4357/aaa95c](https://doi.org/10.3847/1538-4357/aaa95c)